

Predicting Mesoscopic Larmor Frequency Shifts in White Matter with Diffusion MRI - An In-Silico Monte-Carlo Study

Anders Dyhr Sandgaard¹, Sune Nørhøj Jespersen^{1,2}

¹Center of Functionally Integrative Neuroscience, Department of Clinical Medicine, Aarhus University, Denmark

²Department of Physics and Astronomy, Aarhus University, Denmark

Keywords

- 1) Monte-Carlo,
- 2) Magnetic susceptibility,
- 3) Diffusion,
- 4) Larmor frequency,
- 5) Transverse Relaxation,
- 6) Microstructure

Word count: 9973

Corresponding Author: Anders Dyhr Sandgaard.

Mail: anders@cfn.au.dk

Abbreviations: **fODF:** Fiber orientation Distribution Function. **dmMRI:** Diffusion MRI. **SM:** Standard Model of Diffusion in White Matter. **MGE:** Multi-Gradient echo signal. **QSM:** Quantitative Susceptibility Mapping. **STI:** Susceptibility Tensor Imaging. **MC:** Monte-Carlo. **WM:** White Matter. **GM:** Gray Matter. **TBI:** Traumatic Brain Injury. **ASE:** Asymmetric Spin Echo. **PGSE:** Pulsed-Gradient Spin Echo. **EM:** Electron Microscopy. **CC:** Corpus Callosum. **CG:** Cingulum Bundle. **Contra:** Contralateral. **Ipsi:** Ipsilateral. **COM:** Center of mass. **SE:** Spin Echo. **BIC:** Bayesian Information Criterion. **NRMSE:** Normalized Root-Mean-Square-Error. **SD:** Standard Deviation.

1| Abstract

Magnetic susceptibility MRI offers potential insights into the chemical composition and microstructural organization of tissue. However, estimating magnetic susceptibility in white matter is challenging due to anisotropic sub-voxel Larmor frequency shifts caused by axonal microstructure relative to the B₀ field orientation. Recent biophysical models have analytically described how axonal microstructure influences the Larmor frequency shifts, relating these shifts to a mesoscopically averaged magnetic field that depends on the axons' fiber Orientation Distribution Function (fODF), typically estimated using diffusion MRI. This

study aims to validate the use of MRI to estimate mesoscopic magnetic fields and determine whether diffusion MRI can faithfully estimate the orientation dependence of the Larmor frequency shift in realistic axonal microstructure. To achieve this, we developed a framework for performing Monte-Carlo simulations of MRI signals in mesoscopically sized white matter axon substrates segmented with electron microscopy. Our simulations demonstrated that with careful experimental design, it is feasible to estimate mesoscopic magnetic fields. Additionally, the fODF estimated by the Standard Model of diffusion in white matter could predict the orientation dependence of the mesoscopic Larmor frequency shift. We also found that incorporating the intra-axonal axial kurtosis into the Standard Model could explain a significant amount of signal variance, thereby improving the estimation of the Larmor frequency shift. This factor should not be neglected when fitting the Standard Model.

2| Introduction

MRI is a powerful imaging technique sensitive to detecting water diffusion and microscopic magnetic field variations induced by the magnetized tissue^{1,2}. This capability allows examination of tissue at scales significantly finer than the image resolution, enabling observation of voxel-averaged magnetic and microstructural tissue changes. Consequently, MRI is well-suited for detecting minor alterations in brain tissue, which are crucial for studying neurodegeneration. To achieve both sensitive and specific microstructural characterization, biophysical tissue models have been developed to identify subtle tissue changes.

In diffusion MRI (dMRI), the Standard Model of Diffusion in White Matter² (SM), which encompasses a range of previously utilized diffusion models, has become a popular biophysical model in brain tissue research³⁻⁷. Here, the intra-axonal and extra-axonal signal is modelled as Gaussian and non-exchanging compartments for long diffusion times. For example, the intra-axonal signal can be described as a Gaussian signal in a 1D stick compartment, with non-zero diffusivity only along its axis. The total signal from many non-exchanging axon bundles is then modelled as a weighted sum across the axonal directions, governed by a fiber orientation distribution function (fODF) $\mathcal{P}^D(\hat{\mathbf{n}})$. Here, the “D” indicates it is estimated by diffusion MRI. The diffusivities reflect a coarse-grained version of the axonal geometry, while $\mathcal{P}^D(\hat{\mathbf{n}})$ models the orientation of axonal bundles on the mesoscopic scale.

Biophysical models have also been developed to describe how the tissue magnetic susceptibility χ , describing the magnetization response in the presence of an external \mathbf{B}_0 field, shifts the measured Larmor frequency shift $\bar{\Omega}$ of the multi-gradient-echo (MGE) signal⁸⁻¹⁴. On the microscopic scale, susceptibility depends on the chemical composition and molecular structure of cells, providing biomarkers for iron¹⁵⁻²¹, lipid, protein content²²⁻³⁰, etc. The magnetized tissue generates microscopically varying magnetic fields that can shift the Larmor frequency by several hertz in clinical scanners¹⁴. This field depends not only on susceptibility but also on tissue microstructure – encapsulated by the common term *magnetic microstructure*. While diffusion typically probes microstructure on the mesoscopic scale³¹ (10-100 μm), the induced magnetic field is a non-local phenomenon, meaning that the entire tissue sample and its surroundings cause shifts in the spin’s Larmor frequency at every microscopic position in the sample. Even after the massive averaging across the voxel, $\bar{\Omega}$ still contains a mesoscopic contribution $\bar{\Omega}^{\text{Meso}}$ that depends exclusively on local magnetic

microstructure at distances below the imaging resolution. The mesoscopic contribution $\overline{\Omega}^{\text{Meso}}$ can be as significant as the frequency shift induced by tissue from neighboring voxels denoted $\overline{\Omega}^{\text{Macro}}$. Unfortunately, current susceptibility estimation techniques like Quantitative Susceptibility Mapping^{32,33} (QSM) or Susceptibility Tensor Imaging²⁶ (STI) disregard any sub-voxel frequency shift $\overline{\Omega}^{\text{Meso}}$ and assume that the measured signal's Larmor frequency shift can be described by the induced shift $\overline{\Omega}^{\text{Macro}}$ from neighboring voxels. This approximation may appear unavoidable because incorporating microscopic shifts depends on explicit microstructure, leading to more parameters than what is feasible to estimate³⁴ - even after sampling at multiple \mathbf{B}_0 directions. However, if the additional microstructural degrees of freedom, that arise by modelling the sub-voxel frequency shifts, could be known prior to estimating susceptibility, the number of unknowns would be drastically reduced, leaving only a few rotation-invariant susceptibility-related parameters to be estimated^{10,12,14,34}.

Recently, an analytical framework was derived that accounts for both $\overline{\Omega}^{\text{Meso}}$ and $\overline{\Omega}^{\text{Macro}}$ when estimating magnetic susceptibility from MRI^{9,12}. It was shown how $\overline{\Omega}^{\text{Meso}}$ depends on the structural correlation function of the microstructure when susceptibility is uniform. This framework was later used to develop QSM+, which incorporates mesoscopic frequency shifts from multi-layer cylinders with scalar susceptibility and arbitrary orientation dispersion into QSM. Both QSM, QSM+ and STI model the measured Larmor frequency shift in MRI via the voxel-averaged magnetic field described by the first signal cumulant. In QSM+, it was derived how the orientation dependence of the mesoscopic Larmor frequency shift $\overline{\Omega}^{\text{Meso}}$ from dispersed cylinders is captured by a scatter matrix³⁵, $\mathbf{T} = \langle \hat{\mathbf{n}}\hat{\mathbf{n}}^T \rangle$, representing the mean orientation tensor of the cylinder orientations $\hat{\mathbf{n}}$. \mathbf{T} relates to the second moment of the fODF. Utilizing that \mathbf{T} may also be estimated from the fODF with dMRI, it was demonstrated that accounting for $\overline{\Omega}^{\text{Meso}}$ substantially changed susceptibility values in WM in an ex vivo mouse brain.

For an ideal medium of cylinders, the anisotropy of the two different contrast mechanisms (diffusion and magnetic susceptibility) should depend on the same scatter matrix \mathbf{T} . However, real tissue deviates from this ideal picture, and it remains to be investigated how these two “orthogonal” modalities are differently affected by realistic axonal features such as beading, tortuosity, and undulations³⁶. While the two modalities may be influenced by the same structural correlation function, their parameters might be biased differently due to model simplifications. It is therefore timely to investigate if \mathbf{T} from dMRI is similar to \mathbf{T} as seen through susceptibility induced Larmor frequency shifts.

One approach to comparing structural information across multiple MRI modalities is through Monte-Carlo (MC) simulations in realistic tissue phantoms, especially given the advancements in volume microscopy and machine learning for imaging and digitally segmenting large mesoscale tissue samples. Historically, MC simulations in MRI have been used since the 1990s^{37,38} in both artificial substrates and more realistic microscopy images. Over the past two decades, several synthetic media generation methods^{11,37,39–59} have been presented in both white matter (WM) and gray matter (GM), with larger microscopy samples used to validate and investigate diffusion MRI. While the literature covers simulations investigating internal magnetic fields, current studies are limited to using 2D images or considering only a few axons^{11,37,41–43,60–63}. Hence, microstructural information across multiple modalities on the mesoscopic scale has so far not been extensively investigated.

In this study, we use publicly available mesoscale volume microscopy data^{64,65} of rat brain white matter axons. The data, comprising myelinated axon segments from traumatic brain injury (TBI) and SHAM rats, allow us to simulate over 10,000 realistically organized axons simultaneously. Assuming scalar susceptibility, we calculate the magnetic field distribution induced by these axons and perform Monte Carlo simulations to compute MGE signals, asymmetric spin echo (ASE) signals, and pulsed-gradient spin echo (PGSE) signals.

Our objectives are twofold:

1. **Objective 1 (O1):** To determine if MRI can estimate the mesoscopically averaged magnetic field via the phase of the MGE and ASE signals.
2. **Objective 2 (O2):** To evaluate whether our analytical model of cylinders with arbitrary orientation distribution can predict the mesoscopically averaged magnetic field when combined with fODF information estimated with diffusion MRI.

Our work represents an important step towards validating the use of dMRI information to account for sub-voxel frequency shifts caused by the structural anisotropy of WM, which is crucial for robust susceptibility estimation.

3| Methods

Here we give an overview of the WM substrates used to study the effect of the induced magnetic fields $\Delta\mathbf{B}(\mathbf{r})$ from WM axons on the MRI signal, and the MC simulation used to generate MRI signals with and without diffusion weighting. All simulations were done in MATLAB (The Mathworks, Natick, MA, USA) on a desktop PC equipped with a dedicated Nvidia RTX 4070 Ti 12 GB GPU, a 13th generation 16 core Intel i7 processor customized with 192 Gb of DDR5-5200MHz RAM. The code used to process the data, calculate the magnetic fields, and perform MC simulations is available upon reasonable request to the corresponding author.

Processing WM Substrate

We used openly available data of segmented volume electron microscopy (EM) of rat brain WM⁶⁴⁻⁶⁶. We refer to previous studies for a more detailed description of the WM substrates. The data included mesoscopically sized samples of WM with a resolution of 50 nm³. The WM includes corpus callosum (CC) and cingulum bundle (CG) from SHAM rats, and rats undergone traumatic brain injury (TBI). Here we considered eight segmented regions of WM from two SHAM rats (SHAM-25 and SHAM-49) and two TBI rats (TBI-24 and TBI-2), from either the contra-lateral (contra) or ipsilateral (ipsi) side, where the labels are kept in correspondence with the original data. The available MATLAB data contained fully segmented and labelled intra-axonal spaces, and a binary mask of the myelin sheath. Figure 1 gives an overview of the 8 WM substrates.

Prior to calculating the magnetic field and performing MC simulations in these substrates, we made the following refinements to the axons: First, we down sampled the resolution to 0.1 μm^3 . This was necessary for feasible calculation of $\Delta\mathbf{B}(\mathbf{r})$ across the whole sample. The matrix size of the voxelized grid after down-sampling is listed in Table 1. Second, we nulled

all voxels in the intra-axonal space that touched a neighboring axon's intra-axonal space to make sure our MC simulation did not "leak" spins across axons. Third, we performed the following operations iteratively for the intra-axonal space of each segmented axon: We morphologically closed the intra-axonal space to remove any small spurious errors on the surface. Next, we removed all holes in the intra-axonal space, e.g., from segmented cells inside the axons, and checked that each axon consisted of one connected intra-axonal space. If an axon consisted of multiple pieces, we kept only the largest piece. If an axon exhibited branching, the axon was not used for MC, as such typically originated from errors during segmentation. We then computed the center of mass (COM) points for the cross-sectional planes perpendicular to an axon's main direction. Highly curved axons were discarded to simplify the MC simulation. If the axons, for example, were pointing mainly along z , we stored a directional label 3, its direction $\hat{\mathbf{n}}$, and the COM points computed in the xy plane for each z -position. We then checked and removed any touching voxels from different axons. Axons pointing along z were truncated 5 μm above their bottom end due to a visually noticeable systematic curvature that we suspect originated from cutting the tissue sample. If an axon close to the volume boundary touched the side walls of the sample volume, we truncated it such that the whole axon never touched any boundary within the volume and kept only the largest segment. We prepared the ends of the axons such that we could create fully periodic boundaries in our MC simulation, inside the axon, which was crucial to not introduce additional orientation dispersion. This was done by finding two similar (Dice similarity index above 0.9) cross-sectional planes perpendicular to the axon's main direction close to the ends of the axon. We then fused the ends together such that their cross-section was the same. We stored the COM positions of the two ends which were to be used for MC simulations. After all these operations, we calculated the length based on the line following the COM points. Only axons longer than 20 μm was used for MC. Using the toolbox `Rawseg`^{67,68}, we calculated the EM-related fODF $\mathcal{P}^{\text{EM}}(\hat{\mathbf{n}})$ and its expansion coefficients p_{2m}^{EM} in spherical harmonics $Y_l^m(\hat{\mathbf{n}})$

$$\mathcal{P}^{\text{EM}}(\hat{\mathbf{n}}) \approx 1 + \sum_{l=2,4,\dots}^{l_{\max}} \sum_{m=-l}^l p_{2m}^{\text{EM}} Y_l^m(\hat{\mathbf{n}}). \quad (1)$$

This was derived from the axon's COM tangent lines, after coarse graining each line by a Gaussian filter of size $L = \sqrt{6D_0\Delta}$ for different diffusion times of $\Delta = 10, 40, 70$ and 100 ms. We therefore denote $p_{2m}^{\text{EM}}(\Delta)$ as a function of Δ . Lastly, we checked for overlapping voxels one last time, and made sure that the ends remained identical, when considering all the processed axons in the whole grid. The intra-axonal voxels defined an indicator function $v_a(\mathbf{r})$ where \mathbf{r} denotes grid positions. The resulting intra-axonal volume fractions ζ_a for each substrate are listed in Table 1.

Table 1

	Ipsilateral				Contra lateral			
	ζ_a	ζ_m	DIM	#MC Axons	ζ_a	ζ_m	DIM	#MC Axons
SHAM-25	0.12	0.49	1006 × 2035 × 685	14804	0.18	0.49	2028 × 1001 × 646	20594

SHAM-49	0.18	0.48	1003 × 1006 × 598	8496	0.13	0.45	1006 × 2033 × 493	11607
TBI-24	0.10	0.45	1061 × 1453 × 618	10850	0.10	0.50	997 × 2024 × 638	14757
TBI-2	0.07	0.43	1005 × 2034 × 303	7760	0.11	0.47	1008 × 2028 × 536	12831

The original segmented myelin mask was also morphologically closed and small objects were removed. Next, the myelin mask was multiplied by a negated mask of the processed intra-axonal mask, to remove any overlapping voxels. The myelin mask describing the indicator function $v_m(\mathbf{r})$ contained all the original axon's myelin with volume fraction ζ_m as listed in Table 1, and this myelin mask was used to calculate the field distribution, while the labelled grid $v_A(\mathbf{r})$ of intra-axonal spaces of axons longer than 20 μm was used for MC simulations.

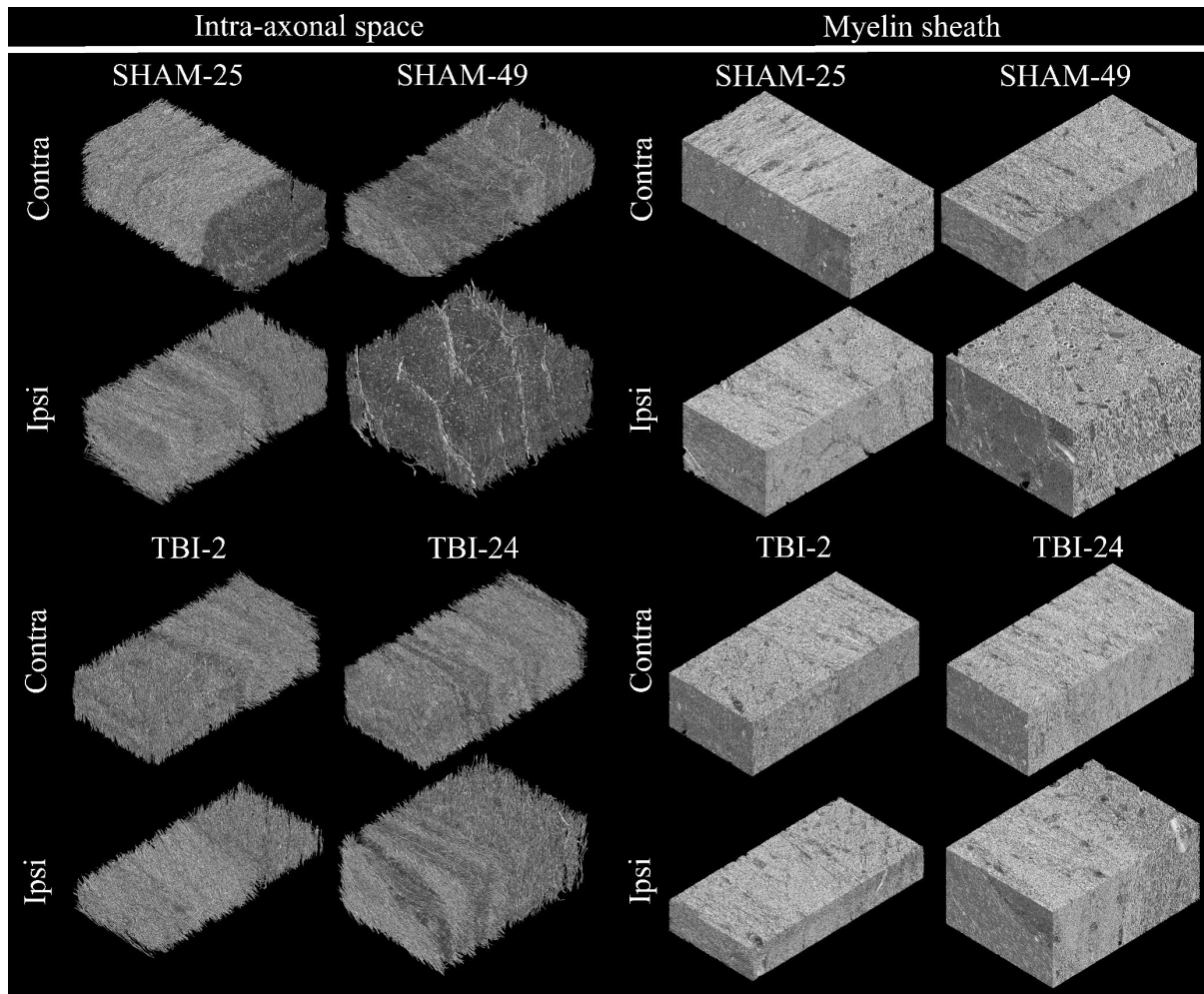


Figure 1 - In-silico white matter axon phantoms used for Monte-Carlo simulations. Eight different substrates were used for Monte-Carlo simulations from two different SHAM rats labelled 25 and 49 and two different TBI rats labelled 2 and 24. Labels correspond to the original data. For each brain, both ipsilateral (ipsi) and contralateral (contra) tissue samples are considered. The tissue is extracted from the corpus callosum and cingulum bundle. The intra-axonal spaces are used for the

Larmor Frequency shift $\Omega(\mathbf{r})$

For our MC simulation we considered signal dephasing due to the (demeaned) Larmor frequency shift $\Omega(\mathbf{r})$ induced by the voxelized susceptibility-weighted myelin grid $\chi_m \nu_m(\mathbf{r})$

$$\begin{aligned}\Omega(\mathbf{r}) &\cong \gamma \hat{\mathbf{B}}^T \Delta \mathbf{B}(\mathbf{r}) = \gamma B_0 \hat{\mathbf{B}}^T \int_V d\mathbf{r}' \mathbf{Y}(\mathbf{r} - \mathbf{r}') \delta\chi_m(\mathbf{r}') \hat{\mathbf{B}} \\ &= \gamma B_0 \hat{\mathbf{B}}^T [\delta\chi \otimes \mathbf{Y}](\mathbf{r}) \hat{\mathbf{B}}.\end{aligned}\quad (2)$$

Here $\delta\chi_m(\mathbf{r}) = \chi_m \nu_m(\mathbf{r}) - \bar{\chi}$ is the zero-mean magnetic susceptibility of the axons, which is computed such that the average Larmor frequency shift across the whole volume V is zero, and $\bar{\chi} = \zeta_m \chi_m$ denotes the mesoscopically averaged magnetic susceptibility. The reason for subtracting the frequency shift from the bulk susceptibility $\bar{\chi}$ is a matter of convention and is done in order to compare the average frequency shift inside the intra-axonal space $\bar{\Omega}_a$ to our previously derived analytical result¹⁴ for the mesoscopic averaged Larmor frequency shift $\bar{\Omega}^{\text{Meso}}$ in a mesoscopic region with zero-mean frequency shift (the frequency shift from $\bar{\chi}$ are instead captured by the so-called macroscopic frequency shift $\bar{\Omega}^{\text{Macro}}$, which is the only shift considered in QSM). We used an intrinsic scalar susceptibility of $\chi_m = -100$ ppb/ ζ_m such that $\bar{\chi} = -100$ ppb agreed with experiments^{14,69,70}. We neglected microscopic susceptibility anisotropy of myelin, firstly because evidence suggests it contributes less than structural anisotropy of axons⁷⁰, and secondly because the EM resolution was inadequate for a faithful simulation. The sample averaged frequency shift $\bar{\Omega}_a$ inside the axons is

$$\bar{\Omega}_a(\mathbf{B}_0) = \frac{1}{V \zeta_a} \int_V d\mathbf{r} \nu_a(\mathbf{r}) \Omega(\mathbf{r}). \quad (3)$$

Here $\Omega(\mathbf{r})$ and $\bar{\Omega}_a(\mathbf{B}_0)$ were computed numerically for the 3D voxelized microstructure in an external magnetic field $\mathbf{B}_0 = B_0 \hat{\mathbf{B}}$, with $B_0 = 3$ T or 7T and 13 different orientations $\hat{\mathbf{B}}$ found using electrostatic repulsion.⁷¹ We thus evaluated our MC simulated MR signal for 26 different frequency distributions in total. For later convenience in our MC simulation, we utilized that every distribution $\Omega(\mathbf{r})$ consists of 6 independent tensor components $\mathbf{A}(\mathbf{r}) \equiv [\delta\chi \otimes \mathbf{Y}](\mathbf{r})$ which can be computed using the convolution theorem and fast Fourier transform, such that $\Omega(\mathbf{r}) = \gamma B_0 \hat{\mathbf{B}}^T \mathbf{A}(\mathbf{r}) \hat{\mathbf{B}}$.

Monte-Carlo simulation

Here we give an overview of the MC simulation performed in the WM substrates. Since this required doing MC simulations in many axons at once, it was crucial that the step and collision type were chosen to make the random walk as computationally simple as possible. Each particle's random step was drawn from a uniform distribution with step length $\delta_l = 0.1$ μm equal to the voxel resolution. The intrinsic diffusivity was set to $D_0 = 2$ $\mu\text{m}^2/\text{ms}$, leading to a time step $\delta_t = 0.83$ μs . When a random walker stepped outside its intra-axonal space, the step was rejected. This rejection sampling scheme led to approximately a 6%

reduction in the intra-axonal axial diffusivity (see Supporting Material), which is acceptable since the orientation distribution is the focus of this study and not the diffusivity. We used on the order of $N \sim 10^7$ particles, corresponding to a particle density of 72 particles/ μm^3 inside the axons. While this is inarguably too few to study diffusion inside individual axons, it was found to robustly estimate the signal from the entire population of axons (see Supporting Material). Performing the MC simulation and computing all the signals for a diffusion time around $\Delta = 100$ ms took around 20 hours per substrate.

MC Signal Generation

The MC simulations were used to simulate a multi gradient echo signal S_{MGE} (MGE), an asymmetric spin echo (ASE) signal S_{ASE} , and a spin-echo (SE) signal with diffusion weighting S_{PGSE} . Figure 2 gives an overview of the encoded signals. To include signal dephasing caused by the varying Larmor frequency $\Omega(\mathbf{r})$, we only had to accumulate a normalized signal tensor $\boldsymbol{\varphi}(T_E; p, t)$ for each random walker p , corresponding to each of the six independent tensor elements in \mathbf{A} , and for each encoded echo time T_E ,

$$\boldsymbol{\varphi}(T_E; p, t) = \alpha_{T_E}(t)\boldsymbol{\varphi}(p, t - 1) + \delta_t \mathbf{A}(\mathbf{r}_p). \quad (4)$$

Here the function

$$\alpha_{T_E}(t) = \begin{cases} 1, & t \neq \frac{T_E}{2} \\ -1, & t = \frac{T_E}{2} \end{cases} \quad (5)$$

specifies when a 180-degree RF pulse (here an ideal phase flip) occurs and \mathbf{r}_p denotes the position of the particle. Numerically, $\boldsymbol{\varphi}$ was stored as an array with dimensions given by the total number of particles, number of echo times T_E and the 6 tensor components of \mathbf{A} . For the MGE signal, $\alpha(t) = 1$ for all t and here we write the normalized signal tensor as $\boldsymbol{\varphi}(p; t)$ for simplicity. The ASE signal $S_{\text{ASE}}(T_E + \Delta T_E)$ at a time $T_E + \Delta T_E$, where ΔT_E denotes the asymmetric delay after T_E , were computed for all combinations $\gamma B_0 \hat{\mathbf{B}}^T \boldsymbol{\varphi}(T_E + \Delta T_E; p) \hat{\mathbf{B}}$ of $\hat{\mathbf{B}}$ and B_0

$$S_{\text{ASE}}(T_E + \Delta T_E) = \frac{1}{N} \sum_p e^{-\gamma B_0 \hat{\mathbf{B}}^T \boldsymbol{\varphi}(T_E + \Delta T_E; p) \hat{\mathbf{B}}} \quad (\text{ASE}), \quad (6)$$

$$S_{\text{MGE}}(t) = \frac{1}{N} \sum_p e^{-\gamma B_0 \hat{\mathbf{B}}^T \boldsymbol{\varphi}(p; t) \hat{\mathbf{B}}} \quad (\text{MGE}).$$

The MGE signal was calculated up to $t = 40$ ms, while the ASE signal was calculated at $T_E = 80$ ms with ΔT_E up to 20 ms.

Pulsed-Gradient diffusion signal S_{PGSE}

We computed the PGSE signal S_{PGSE} by adding a diffusion gradient \mathbf{g} to the SE signal encoding, see Figure 2 for an overview. The gradient \mathbf{g} was chosen such that $b = 0, 1, 3, 4, 5, 7, 10$ ms/ μm^2 and with $\hat{\mathbf{g}}$ along 30 gradient directions for $b < 5$ ms/ μm^2 , and 60 directions for the remaining. The directions were selected using electrostatic repulsion⁶³. The

diffusion time was either $\Delta = 10, 40, 70, 100$ ms, while the gradient pulse duration was equal to the time step, $\delta = \delta_t$. The echo time considered for the PGSE signal was $T_E = 15\text{ms} + \Delta$ to minimize computation time. Then, to compute the signal $S(b, \hat{\mathbf{g}})$, we first compute the contribution to particle p 's signal phase from the diffusion weighting as $\gamma\delta_t\sqrt{b/(\Delta - \delta/3)}\hat{\mathbf{g}} \cdot \Delta\mathbf{I}_p$ and then calculate the sum

$$S_{\text{PGSE}}(b, \hat{\mathbf{g}}) = \frac{1}{N} \sum_p e^{-i\gamma B_0 \hat{\mathbf{B}}^T \varphi(T_E; p) \hat{\mathbf{B}} - i\gamma\delta_t\sqrt{b/(\Delta - \delta/3)}\hat{\mathbf{g}} \cdot \Delta\mathbf{I}_p} \quad (\text{PGSE}). \quad (7)$$

Notice $S_{\text{PGSE}}(0) = S_{\text{ASE}}(T_E)$ when $b = 0$.

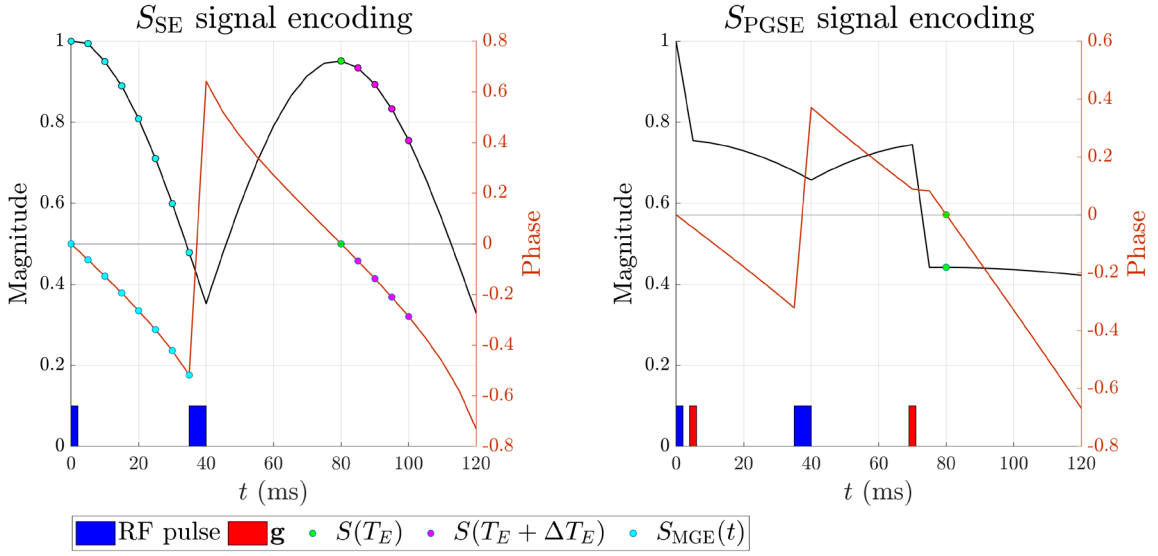


Figure 2 – Signal encoding for SHAM-25-ipsi. Left figure shows encoding of spin echo signal. Blue tiles indicate the 90-degree and 180-degree RF pulse. Cyan point shows the measurement of the gradient echo signal, here up to $t = 40$ ms. Green point show spin echo signal at the echo time, here $T_E = 80$ ms, while magenta points indicate measuring the spin echo signal at a later time, here up to $\Delta T_E = 20$ ms. Right figure shows encoding of PGSE signal. Red tiles indicate the pulsed gradients.

Parameter estimation

The Standard Model of diffusion in WM

For long diffusion times, the signal from a single non-exchanging axon with orientation $\hat{\mathbf{n}}$ is typically modelled by a gaussian stick compartment² (zero radial diffusivity). The signal kernel from a bundle of parallel sticks is thus

$$\mathcal{K}(b, \hat{\mathbf{n}} \cdot \hat{\mathbf{g}}) = e^{-bD_a(\hat{\mathbf{n}} \cdot \hat{\mathbf{g}})^2}, \quad (\text{Stick compartment}). \quad (8)$$

For a collection of non-exchanging stick bundles with different orientations, the total signal is obtained by a convolution with the fODF $\mathcal{P}^D(\hat{\mathbf{n}})$, where the superscript ‘D’ for “diffusion” is to distinguish it from the EM-derived fODF, \mathcal{P}^{EM} :

$$S_{SM}(b, \hat{\mathbf{g}}) = S_0 \int d\hat{\mathbf{n}} \mathcal{P}^D(\hat{\mathbf{n}}) \mathcal{K}(b, \hat{\mathbf{n}} \cdot \hat{\mathbf{g}}). \quad (9)$$

The fODF $\mathcal{P}^D(\hat{\mathbf{n}})$ can also be expanded in spherical harmonics $Y_l^m(\hat{\mathbf{n}})$

$$\mathcal{P}^D(\hat{\mathbf{n}}) \approx 1 + \sum_{l=2,4,\dots}^{l_{\max}} \sum_{m=-l}^l p_{lm}^D Y_l^m(\hat{\mathbf{n}}), \quad (10)$$

where p_{lm}^D are the diffusion-derived fODF expansion coefficients. In practice, the apparent fODF and thus the p_{lm}^D depend on the diffusion time⁶⁷, and so we write $p_{lm}^D(\Delta)$.

We also consider $S_{SM}(b, \hat{\mathbf{g}})$ with an intra-axonal axial kurtosis⁷² W_a^{\parallel} , such that the kernel becomes

$$\mathcal{K}(b, \hat{\mathbf{n}} \cdot \hat{\mathbf{g}}) = e^{-bD_a(\hat{\mathbf{n}} \cdot \hat{\mathbf{g}})^2 + \frac{1}{6}(bD_a)^2(\hat{\mathbf{n}} \cdot \hat{\mathbf{g}})^4 W_a^{\parallel}}, \quad (\text{Stick with axial kurtosis}). \quad (11)$$

Upon fitting $S_{SM}(b, \hat{\mathbf{g}})$ to the MC simulated PGSE signal S_{PGSE} , we computed the difference in the Bayesian information criterion⁷³ ΔBIC to check the change in residual variance compared to adding an additional parameter. A difference of $\Delta\text{BIC} < -6$ would support a non-vanishing W_a^{\parallel} .⁷⁴

Mesoscopic Larmor frequency shift from cylinders with arbitrary orientation distribution

One of the main goals of this study was to compare $\bar{\Omega}_a(\mathbf{B}_0)$ with our previously derived analytical result¹⁴

$$\bar{\Omega}^{\text{Meso}}(\mathbf{B}_0) = -\gamma B_0 \bar{\chi} \frac{1}{2} \left(\mathbf{T}(\hat{\mathbf{B}}) - \frac{1}{3} \right) \quad (12)$$

for the mesoscopically averaged Larmor frequency shift $\bar{\Omega}^{\text{Meso}}$ for long multi-layered cylinders with scalar susceptibility and arbitrary orientation dispersion. Equation (12) is valid for both the average intra-axonal and average extra-axonal frequency shifts (the latter not considered here). Here $\mathbf{T}(\hat{\mathbf{B}}) = \hat{\mathbf{B}}^T \mathbf{T} \hat{\mathbf{B}}$ where \mathbf{T} is the fODF scatter matrix³⁵, which can be written in terms of the $l=2$ expansion coefficients p_{2m}^{Ω} of the ODF in spherical harmonics Y_2^m

$$\mathbf{T}(\hat{\mathbf{B}}) = \hat{\mathbf{B}}^T \mathbf{T} \hat{\mathbf{B}} = \frac{1}{3} + \frac{2}{15} \sum_{m=-2}^2 p_{2m}^{\Omega} Y_2^m(\hat{\mathbf{B}}). \quad (13)$$

Notice we write p_{2m}^{Ω} to distinguish it from $p_{2m}^{\text{EM}}(\Delta)$ and $p_{2m}^{\text{D}}(\Delta)$, and is independent of diffusion time as $\bar{\Omega}^{\text{Meso}}$ describes the mean magnetic field¹³.

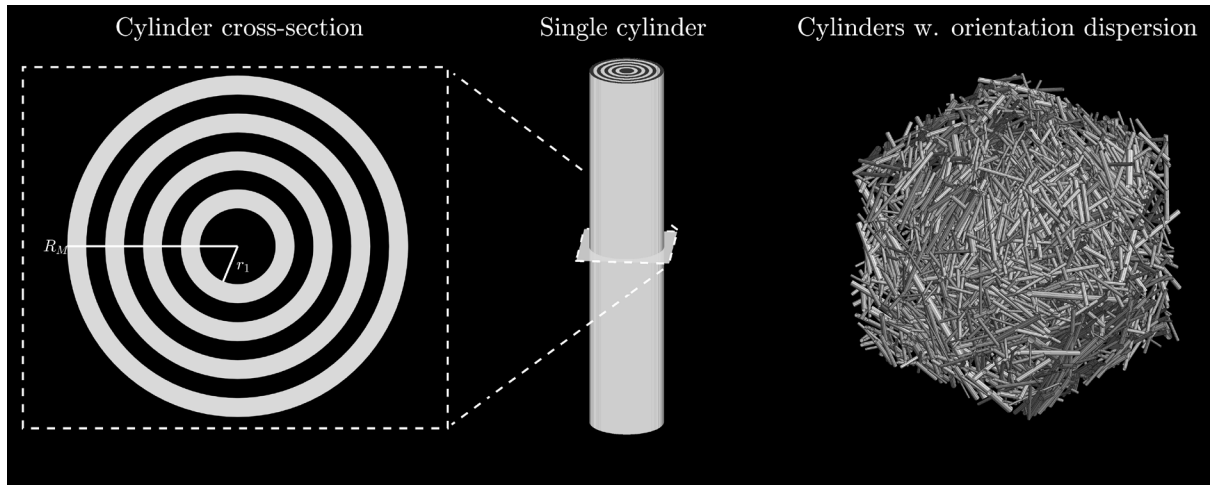


Figure 3 – Biophysical model of WM axons as long hollow cylinders randomly positioned and with arbitrary orientation dispersion. Cylinders are assumed to have a scalar magnetic susceptibility χ_m .

Analysis

Equation (12) was developed as a biophysical model of the measured frequency shift from myelinated axons based on infinitely long cylinders (see Figure 3). However, it remains to be validated. Since we cannot estimate p_{2m}^{Ω} solely from MGE data, where $\bar{\chi}$ is unknown, a central question is if $p_{2m}^{\text{D}}(\Delta) \approx p_{2m}^{\Omega}$ to a sufficient degree to accurately estimate $\bar{\Omega}_a(\mathbf{B}_0)/\bar{\chi}$ from $\bar{\Omega}^{\text{Meso}}(\mathbf{B}_0; \Delta)/\bar{\chi}$ and $p_{2m}^{\text{D}}(\Delta)$. This, in turn, would support the estimation of $\bar{\chi}$ for this particular microstructure with QSM+, an extension of QSM that incorporates sub-voxel frequency shifts from orientationally dispersed axons described by Eq. (12), and where the $p_{2m}^{\text{D}}(\Delta)$ are used to estimate $\mathbf{T}(\hat{\mathbf{B}})$ prior to susceptibility fitting. We therefore performed the following comparisons:

O1)

We investigated at what gradient echo times the slope of the simulated MGE signal $S_{\text{MGE}}(t)$ phase agreed with the intra-axonal frequency shift $\bar{\Omega}_a(\mathbf{B}_0)$ generated by the induced magnetic field. This was to ensure that $\bar{\Omega}_a(\mathbf{B}_0)$ can be meaningfully measured from MR. We fitted the measured signal phase of $S_{\text{MGE}}(t)$ using time points up to a given t_{max} up to 40 ms using either a linear or a 3rd order polynomial fit. The linear coefficient in either case was then compared to $\bar{\Omega}_a(\mathbf{B}_0)$ for varying $\hat{\mathbf{B}}$ and B_0 . We also investigated the signal phase of $S_{\text{ASE}}(T_E + \Delta T_E)$, with $T_E = 40$ ms and $(\Delta T_E)_{\text{max}}$ up to 20 ms and performed the same comparison.

O2)

Next step was to compare $\bar{\Omega}_a(\mathbf{B}_0)$ against $\bar{\Omega}^{\text{Meso}}(\mathbf{B}_0; \Delta)$ where $\mathbf{T}(\hat{\mathbf{B}})$ was estimated using $\bar{\chi}$ and either $p_{2m}^{\text{D}}(\Delta)$ or $p_{2m}^{\text{EM}}(\Delta)$, i.e.

$$\bar{\Omega}_{\text{EM}}^{\text{Meso}}(\mathbf{B}_0; \Delta) = -\gamma B_0 \bar{\chi} \frac{1}{15} \sum_{m=-2}^2 p_{2m}^{\text{EM}}(\Delta) Y_2^m(\hat{\mathbf{B}}), \quad (14)$$

and

$$\bar{\Omega}_{\text{D}}^{\text{Meso}}(\mathbf{B}_0; \Delta) = -\gamma B_0 \bar{\chi} \frac{1}{15} \sum_{m=-2}^2 p_{2m}^{\text{D}}(\Delta) Y_2^m(\hat{\mathbf{B}}). \quad (15)$$

To test how well the fODF from EM and diffusion, respectively, could be used for estimating susceptibility, we computed the normalized root-mean-square-error (NRMSE) across $\hat{\mathbf{B}}$ as a function of the diffusion time Δ

$$\text{NRMSE}_{\text{EM}}(\Delta) = \frac{\sqrt{\frac{1}{N_{\hat{\mathbf{B}}}} \sum_{\hat{\mathbf{B}}} \left(\bar{\Omega}_{\text{EM}}^{\text{Meso}}(\mathbf{B}_0; \Delta) - \bar{\Omega}_a(\mathbf{B}_0) \right)^2}}{\max(\bar{\Omega}_a(\mathbf{B}_0)) - \min(\bar{\Omega}_a(\mathbf{B}_0))} \quad (16)$$

and

$$\text{NRMSE}_{\text{D}}(\Delta) = \frac{\sqrt{\frac{1}{N_{\hat{\mathbf{B}}}} \sum_{\hat{\mathbf{B}}} \left(\bar{\Omega}_{\text{D}}^{\text{Meso}}(\mathbf{B}_0; \Delta) - \bar{\Omega}_a(\mathbf{B}_0) \right)^2}}{\max(\bar{\Omega}_a(\mathbf{B}_0)) - \min(\bar{\Omega}_a(\mathbf{B}_0))} \quad (17)$$

Here we chose to normalize the RMSE to the range, $\max(\bar{\Omega}_a(\mathbf{B}_0)) - \min(\bar{\Omega}_a(\mathbf{B}_0))$, since $\bar{\Omega}_a(\mathbf{B}_0)$ takes on both positive and negative values.

We also estimated the error ratio β by minimizing the least squares difference across $\hat{\mathbf{B}}$ as a function of the diffusion time Δ

$$\beta_{\text{EM}}(\Delta) = \frac{1}{\bar{\chi}} \underset{\bar{\chi}'}{\operatorname{argmin}} \frac{1}{2} \sum_{\hat{\mathbf{B}}} \left(\bar{\Omega}_{\text{EM}}^{\text{Meso}}(\mathbf{B}_0; \Delta, \bar{\chi}') - \bar{\Omega}_a(\mathbf{B}_0) \right)^2, \quad (18)$$

and

$$\beta_{\text{D}}(\Delta) = \frac{1}{\bar{\chi}} \underset{\bar{\chi}'}{\operatorname{argmin}} \frac{1}{2} \sum_{\hat{\mathbf{B}}} \left(\bar{\Omega}_{\text{D}}^{\text{Meso}}(\mathbf{B}_0; \Delta, \bar{\chi}') - \bar{\Omega}_a(\mathbf{B}_0) \right)^2. \quad (19)$$

Hence, $\beta = 1$ corresponds to a perfect susceptibility fit.

4| Results

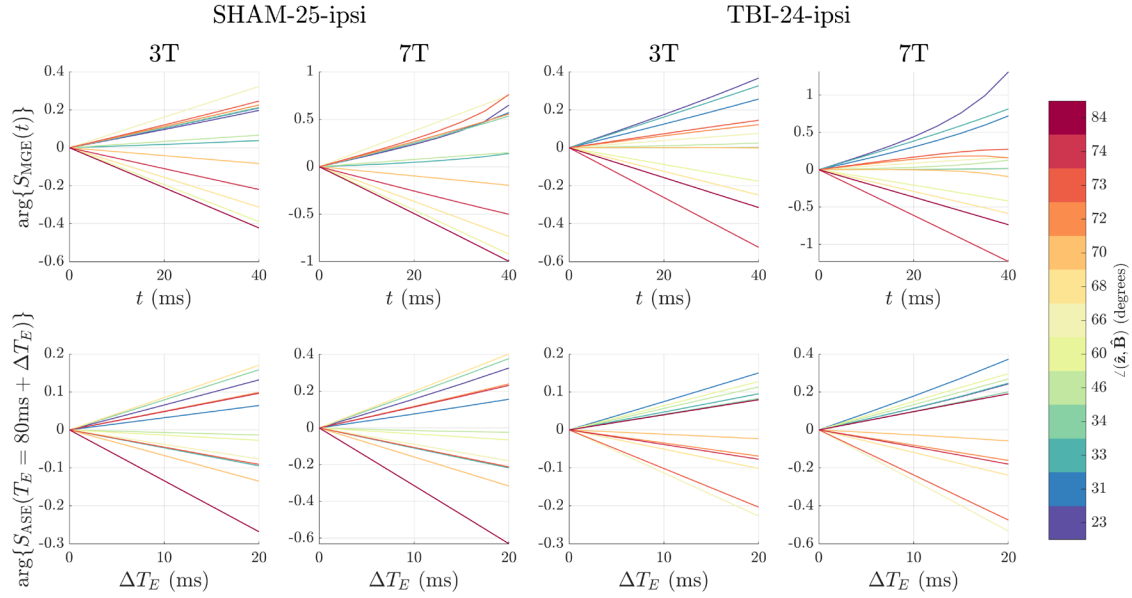


Figure 4 – Upper row shows the signal phase, $\arg\{S_{MGE}(t)\}$, of the MGE signal with an external field of either 3T or 7T for SHAM-25-ipsi and TBI-24-ipsi. Second row shows the phase $\arg\{S_{ASE}(T_E + \Delta T_E)\}$ with $T_E = 80ms$. Colors corresponds to different angles between \mathbf{B}_0 and $\hat{\mathbf{z}}$.

O1)

Figure 4 shows the MC signal phase for SHAM-25-ipsi of $S_{MGE}(t)$ and $S_{ASE}(T_E + \Delta T_E)$ for each field strength and direction. At 3T, very few directions exhibited non-linear behavior, which became more evident at 7T for $S_{MGE}(t)$. This shows that even though the signal comes from roughly 10,000 non-exchanging compartments, and could therefore have been expected to contain higher-order cumulants proportional to the population variance of the Larmor frequency, the signal phase remained fairly linear. As described in a previous study¹⁴, as time increases, and transverse relaxation in each compartment becomes more pronounced, the phase is well described by a power series in time, and the mean magnetic field may still be measurable by the linear term from a polynomial fit.

Figure 5 shows the mean ratio $\left\langle \frac{\bar{\Omega}_{MGE}(\mathbf{B}_0)}{\bar{\Omega}_a(\mathbf{B}_0)} \right\rangle_{\hat{\mathbf{B}}}$ and standard deviation (SD) between the linear term $\bar{\Omega}_{MGE}(\mathbf{B}_0)$ found from fitting the MC-simulated MGE signal phase to either a linear or 3rd order polynomial, and $\bar{\Omega}_a(\mathbf{B}_0)$. Both the mean and standard deviation are calculated over the $\hat{\mathbf{B}}$ directions, and the ratio is shown for different maximum times t_{max} used in the fit. For 3T, linear fitting produced good results with a mean error $100\% \cdot \left(1 - \left\langle \frac{\bar{\Omega}_{MGE}(\mathbf{B}_0)}{\bar{\Omega}_a(\mathbf{B}_0)} \right\rangle_{\hat{\mathbf{B}}}\right)$, and SD within 2% across all substrates, except TBI-24-ipsi that had an SD of 30%. The error was even further reduced by fitting a 3rd order polynomial, resulting in an SD of 5% for TBI-24-ipsi. At 7T, the 3rd order polynomial fitting again produced the

best result. However, the mean error and standard deviation depended greatly on the microstructure. In SHAM-49-ipsi, which only contained cingulum, the mean error was still within 2% and SD around 4% for both linear and 3rd order fitting. Conversely, TBI-24-ipsi had an SD close to 110% for $t_{\max} = 40$ ms. This was however reduced to an SD of 20% and mean of 7% by doing 3rd order fitting and using $t_{\max} < 30$ ms.

We also considered a different approach of using instead the phase of the asymmetric spin echo $\bar{\Omega}_{\text{ASE}}$ at times ΔT_E after the echo T_E . Figure 6 shows the mean ratio $\langle \bar{\Omega}_{\text{ASE}}(\mathbf{B}_0) / \bar{\Omega}_a(\mathbf{B}_0) \rangle_{\mathbf{B}}$ between the linear term $\bar{\Omega}_{\text{ASE}}(\mathbf{B}_0)$, found from fitting the MC simulated ASE signal phase after $T_E = 80$ ms to either a linear or 3rd order polynomial, and $\bar{\Omega}_a(\mathbf{B}_0)$. The ratio is shown for different maximum times $(\Delta T_E)_{\max}$ included in the fit. Here we found the third order polynomial fitting to perform best, making the mean ratio less than 5% for all substrates. For TBI-25-ipsi the SD was reduced to 12%.

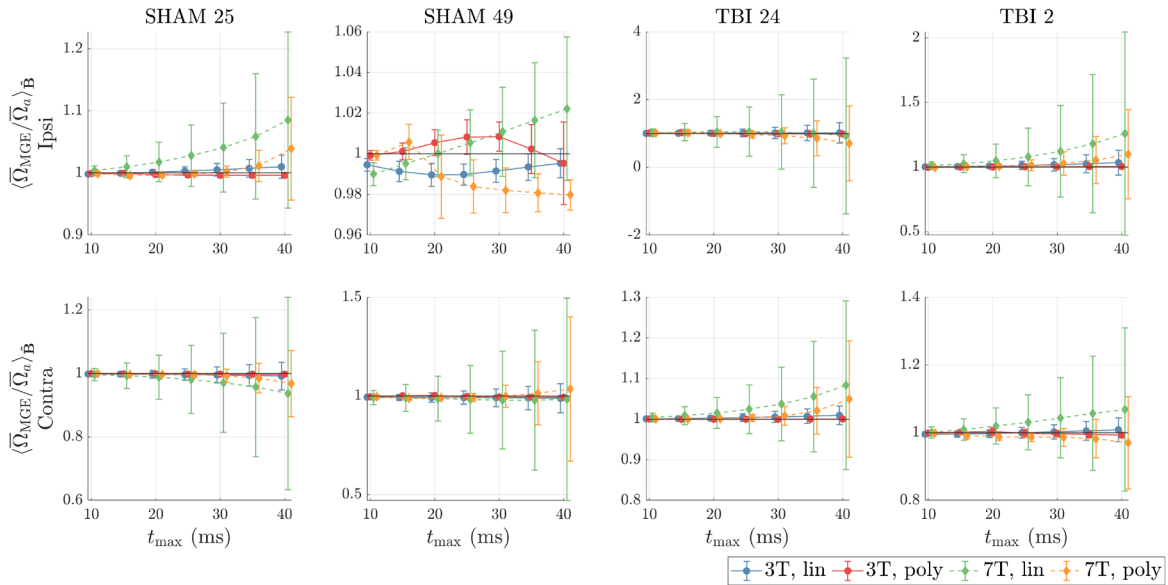


Figure 5 – Error ratio from fitting a linear or 3rd order polynomial to the phase of the MC simulated MGE signal S_{MGE} . Figure shows for SHAM-25-ipsi. First row shows fitting when the external field is $B_0 = 3\text{T}$, while the second row shows for 7T. The x-axis indicates the maximum time used in the fit. The colors indicate different field strength and fit (see legend).

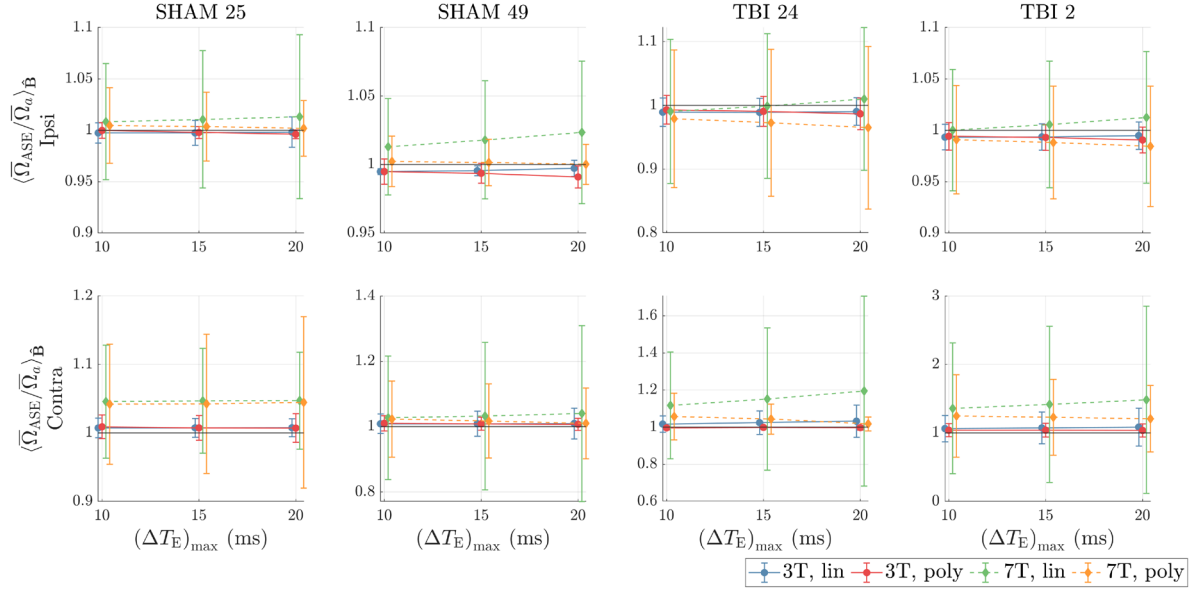


Figure 6 – Error ratio from fitting a linear or 3rd order polynomial to the phase of the MC simulated SE signal S_{SE} at times ΔT_E after the echo $T_E = 80$ ms. The first row shows fitting ipsilateral substrates, while bottom row shows contralateral substrates. The rows correspond to different rat brains. Colors indicate different fitting protocols and field strengths. The x-axis indicates the maximum time used to fit the phase.

O2)

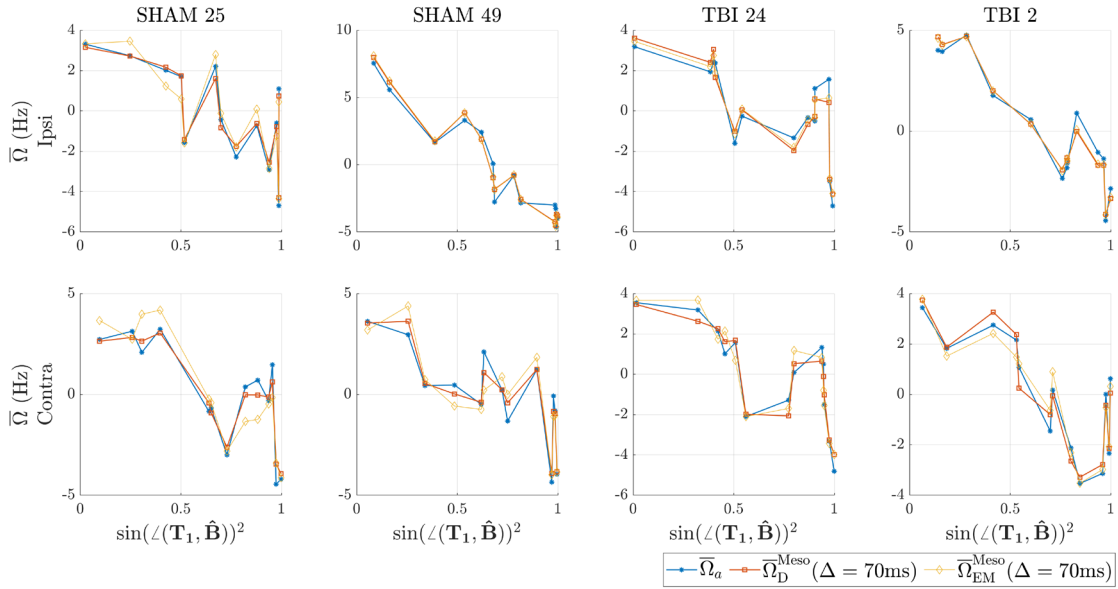


Figure 7 – Larmor frequency shift for different WM substrates. Blue curve shows the intra-axonal frequency shift $\bar{\Omega}_a$ described by the mean magnetic field, while the red shows the estimated Larmor frequency shift $\bar{\Omega}_D^{Meso}$ based on the model for dispersed cylinders and estimated using the fODF estimated from MC simulated diffusion MRI signal with diffusion time $\Delta = 70$ ms. The x-axis shows \sin^2 to the angle between the external field $\hat{\mathbf{B}}$ and the principal eigenvector \mathbf{T}_1 of the scatter matrix \mathbf{T} .

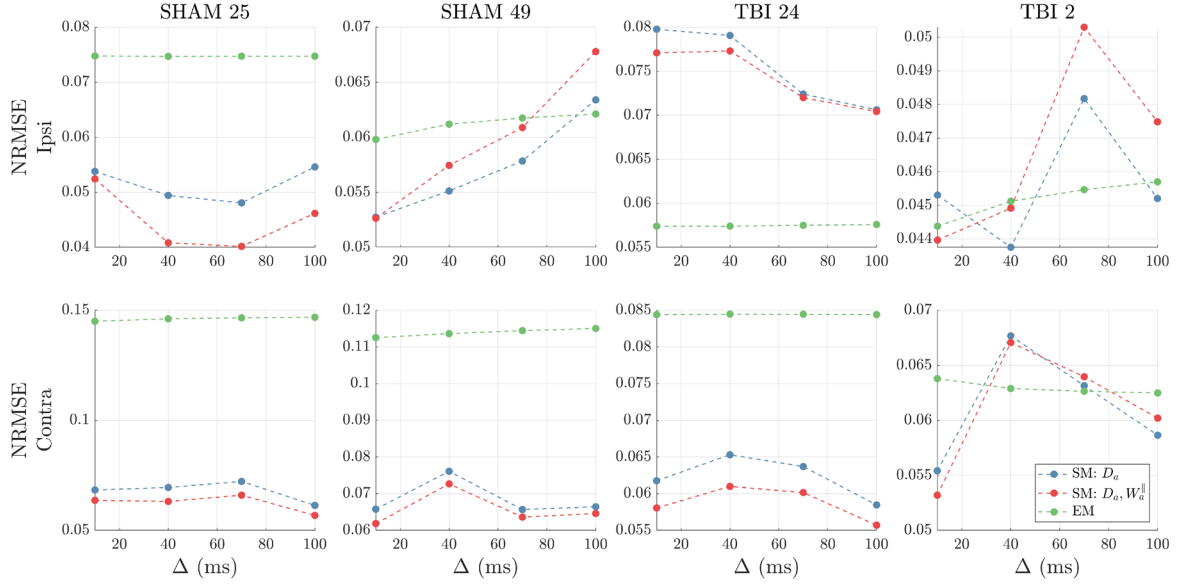


Figure 8 – Normalized RMSE (NRMSE) between the simulated frequency shift $\bar{\Omega}_a$ and the theoretical mesoscopic frequency $\bar{\Omega}^{\text{Meso}}$ (cf. Eqs. (14)-(15)) estimated by using the fODF from fitting the standard model of diffusion to the simulated PGSE signal (blue and red) or using the fODF estimated directly from the EM data (in green). SM model fitting was done with (red) and without (blue) including intra-axonal axial kurtosis. The x-axis indicates the times Δ between the gradient pulses for the PGSE signal, or the time determining the size of the Gaussian filter ($\sqrt{2D_a\Delta}$) used to smooth the center of mass lines of each axon. Two first columns show for SHAM rats while the third and fourth column show for TBI rats.,

Figure 7 shows $\bar{\Omega}_a(\mathbf{B}_0)$ and $\bar{\Omega}^{\text{Meso}}(\mathbf{B}_0; \Delta)$ across the different angles $\angle(\mathbf{T}_1, \hat{\mathbf{B}}) = \arccos(\mathbf{T}_1 \cdot \hat{\mathbf{B}})$ between \mathbf{B}_0 and the principal eigenvector \mathbf{T}_1 of the estimated fODF scatter matrix. Here $B_0 = 7 \text{ T}$.

Figure 8 shows the NRMSE (cf. Eqs. (16)-(17)) using the fODF estimated from EM or the fODF estimated from diffusion by fitting SM with or without axial kurtosis W_a^{\parallel} . In the figure, the internal fields were induced by an external field strength $B_0 = 7 \text{ T}$, but similar SM fitting results were found for 3T, and without internal fields, indicating a low bias in fODF estimation due to internal fields. For all substrates and across all diffusion times Δ , the NRMSE was around 5-8%, demonstrating a good correspondence between the first frequency shift $\bar{\Omega}_a(\mathbf{B}_0)$ and the model-based estimation $\bar{\Omega}^{\text{Meso}}(\mathbf{B}_0; \Delta)$ cf. Eq. (12). This is also evident from Figure 8.

Figure 9 shows the fitted β -values, $\beta_D(\Delta)$ and $\beta_{EM}(\Delta)$ (cf. Eqs. (18)-(19)) for different diffusion times. Here we found that $\beta_D(\Delta)$ was less 10% for $\Delta \geq 70 \text{ ms}$, across all substrates, if W_a^{\parallel} was included. This shows that accounting for W_a^{\parallel} for the intra-axonal signal may be important when estimating the fODF from diffusion MRI.

Figure 10 shows the estimated SM parameters along with the difference ΔBIC , from fitting all 8 substrates with and without W_a^{\parallel} . All parameters clearly change across all substrates, and the residual variance between the estimated and MC-simulated signal drops substantially when adding W_a^{\parallel} , which is reflected in a ΔBIC between -250 to -25 for the SHAM substrates and -500 to -200 for TBI substrates. Hence, the importance of accounting for W_a^{\parallel} may depend on the axon morphology which changes due to TBI⁶⁶.

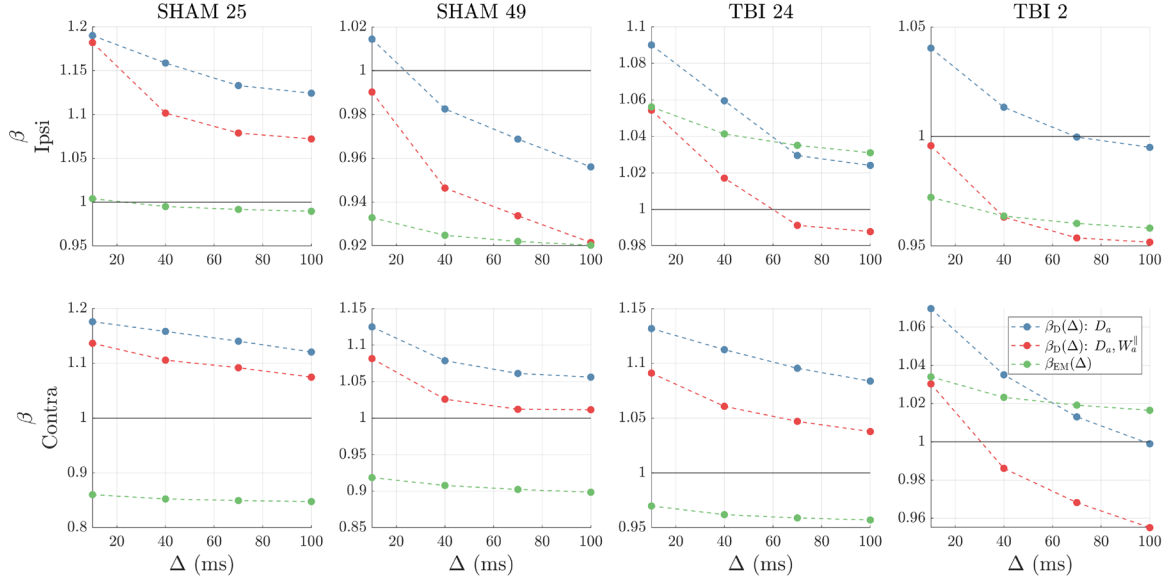


Figure 9 – Normalized susceptibility fitting parameter β for all WM substrates. β was estimated by minimizing the squared difference between the frequency shift $\overline{\Omega}_\alpha$ corresponding to the mean intra-axonal magnetic field and the estimated mesoscopic frequency $\overline{\Omega}^{Meso}$. The frequency was estimated using the fODF from fitting the standard model of diffusion to the simulated PGSE signal (blue and red) or using the fODF estimated directly from the EM data (in green). SM model fitting was done with and without intra-axonal axial kurtosis W_a^{\parallel} . The x-axis shows the time Δ controlling the width of the coarse graining filter, and corresponds either to the time between the gradient pulses for the PGSE signal (for diffusion) or the size of the Gaussian filter used to smooth the center of mass lines of each axon (for EM).

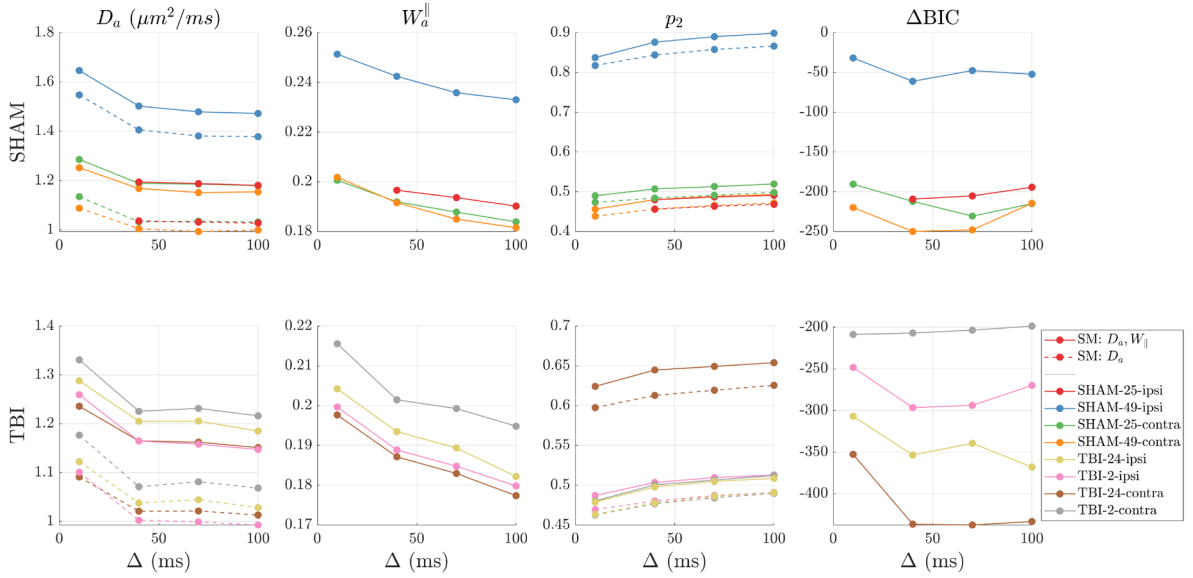


Figure 10 – Fitted Standard model (SM) parameters for all eight substrates. The upper row shows parameters of SHAM rats and the lower row TBI rats. The colors correspond to the different substrates. Solid lines correspond to fitting SM with axial kurtosis, while dashed shows without (conventional SM). The upper row shows intra-axonal diffusivity D_a and kurtosis W_a^{\parallel} , while the second row shows the dispersion parameter p_2 and the difference in Bayesian Information Criteria ΔBIC . We excluded the first red point at $\Delta = 10$ ms as the fit did not prove stable there, and the values became unrealistic.

5| Discussion

Implications of realistic WM microstructure for the estimation of magnetic susceptibility

In this work, we studied how the MRI signal depends on realistic WM axonal microstructure. This was done by performing Monte-Carlo (MC) simulations of the MRI signal for intra-axonal water in mesoscopically sized in-silico WM axon substrates from rat brain obtained from 3D electron microscopy^{64,65}. Here we investigated if the orientation dependence of the multi gradient echo and asymmetric spin echo signal phases could be captured using information from diffusion MRI (dMRI). The connection to dMRI was recently described in our model framework, QSM+, which models the Larmor frequency shift from myelinated axons as orientationally dispersed concentric cylinders with scalar susceptibility.¹⁴ In this model, the orientation dependence is captured by the $l=2$ expansion coefficients p_{2m}^Ω of the cylinders' fiber orientation distribution function (fODF). Here we tested if the fODF estimated from dMRI could be used in our analytical solution for the mesoscopic frequency shift to predict the simulated signal phase. We therefore simulated a PGSE signal and fitted the Standard Model of Diffusion in White Matter (SM) to estimate p_{2m}^D of the diffusion-derived fODF. Our results showed that incorporating p_{2m}^D into QSM+ could predict the measured mesoscopic frequency shift in the intra-axonal space from realistic WM axons with scalar susceptibility. This result was reproducible across four different substrates from SHAM rats and four different substrates from rats undergone Traumatic Brain Injury (TBI). Deviations between p_{2m}^D and p_{2m}^Ω will inevitably arise since p_{2m}^D was determined solely from the intra-axonal spaces of the axons used for MC, while p_{2m}^Ω comes from the mean shift inside the same intra-axonal spaces, but induced by all axons' myelin sheath – including the ones not used for MC. The reason for using all axon's myelin sheath was that the density of axons was not uniform over the whole volume, resulting in a non-uniform bulk susceptibility inside the sample. However, in QSM+, it is assumed that the bulk susceptibility is constant across the mesoscopic volume (voxel in practice), and this requirement was better fulfilled by retaining the realistic density of axons across the volume.

Implications of realistic WM microstructure for the estimation of Standard Model parameters

Previous studies have shown that SM parameters correlated with histological features of these axon substrates⁶⁶. Our simulations also demonstrate that for realistic diffusion times, intra-axonal axial kurtosis affects the measured PGSE signal, and may need to be accounted for to estimate the fODF. This was evident based on improvement in fODF estimation, non-negligible differences in SM parameters, and a lower Bayesian information criterion compared to having only an intra-axonal axial diffusivity. For example, including W_a^\parallel increased the intra-axonal diffusivity D_a around 10-20%. We also tried adding a non-zero radial diffusivity, but this could not explain enough signal variance to be justified based on the Bayesian information criterion. As described in previous studies⁶⁸, and reproduced here (see appendix), axon morphology such as caliber variation, tortuosity, etc., makes W_a^\parallel decay as a power law, and for realistic diffusion times, it can produce a non-negligible effect on the diffusion signal. Based on our results, we therefore recommend to consider W_a^\parallel when fitting SM.

Limitations and future extensions

Our study focused exclusively on the effects of microstructure with scalar susceptibility on the MRI signal phase. However, we did not account for susceptibility anisotropy of myelin or other potential field perturbing sources such as iron-filled neuroglia.⁷⁵ For example, previous simulations⁷⁶ of the field from orientationally dispersed cylinders with susceptibility anisotropy, even for perfect cylinders discretized on a 3D grid with high resolution led to an error of around 5% compared to analytical results. We have previously shown how spheres may also play an important role in the measured frequency shift⁷⁶, as their positions can correlate with the axons both inside and outside the axons. However, if the sources have sufficiently high magnetic susceptibility, a different model picture accounting for strong static dephasing⁸ may be necessary. We therefore plan to add additional complexity to the simulation in the future, e.g., by utilizing other publicly available EM data with segmented neuroglia, vessels and other relevant structures.⁷⁷

We only considered the intra-axonal signal here for several reasons. First, preparing the tissue for EM may alter the geometry of the extra-axonal space. Also, the extra-axonal space has a complex boundary, which makes appropriate boundary conditions difficult to implement.

Diffusion-weighting

Here we simulated diffusion weighting with ideal pulsed diffusion gradients and a perfect 180-degree RF pulse. While this differs from a real measurement, our simulations provide important first insights into the dMRI signal from such a large mesoscopic in-silico sample. Future work will extend the simulation to include realistic diffusion gradient shapes, but also B-tensor encoding like double diffusion encoding⁷⁸. Recent studies have also demonstrated the potential of using diffusion weighting to filter different axonal bundles according to their orientation to the external magnetic field.⁷⁶ Given the natural orientation dispersion of axons, this approach may enable estimating orientation dependent transverse relaxation across echo times T_E , and the signal dephasing and transverse relaxation as functions of the delay time ΔT_E of the asymmetric spin echo sampled at times after T_E . While this has so far been validated for ideal cylinder phantoms⁷⁶, it has not been investigated in realistic substrates. We therefore intend to investigate this approach using this MC simulation framework in a future study.

Computational demand

The random walk simulation was carried out in double precision as high diffusion times led to catastrophic cancellation in single precision. However, the internal field tensor $\boldsymbol{\varphi}$ could be stored in single precision, which allocated around 32 Gb RAM. For the MC simulation, this meant phase accumulation due to internal fields had to be carried out on the CPU rather than GPU, as our desktop GPU only had 12Gb of memory. A more powerful GPU could therefore speed up the computation time substantially. Allocating the full frequency tensor $\mathbf{A}(\mathbf{r})$ allows for fast extraction of values, as particle positions can be converted into an index position in the array. This basically makes finding the added phase for every particle a single operation. As the frequency shift is only considered inside axons, the low axonal volume fraction of approximately 15% made the problem somewhat sparse. However, only storing non-zero values require storing their index. This means that each particle position must be matched

with the correct index in the array, resulting in two operations (a search and an extraction), ultimately leading to higher computation time in comparison to storing the full array, and directly extracting the values. However, better methods might be possible (e.g., utilizing the Cusparse library in CUDA), but this was not pursued here.

Propositions for QSM and STI

Here we showed that estimating the mean magnetic field from the gradient echo signal $S_{\text{MGE}}(t)$ must be done with consideration of the magnetic field strength and readout times. The best estimation achieved in our study for 7T was for times less than 30 ms; at 3T, on the other hand, we could successfully estimate the mean magnetic field for all times considered. However, since myelin water likely affects the Larmor frequency shift at low echo times^{79–82}, it is favorable to measure $S_{\text{MGE}}(t)$ at times longer than the transverse relaxation time of myelin water. This is necessary as long as a complete model of myelin water remains unsolved⁸³. Since measuring $S_{\text{MGE}}(t)$ for long echo times (cf. Figure 5) might hamper estimating the mean magnetic field directly, we found that a better strategy may be to instead perform a spin echo experiment with high T_E , and then sample its decay, e.g., by sampling an asymmetric spin echo at times ΔT_E . As shown in Figure 6, this greatly improved estimation of the mean magnetic field. However, using this approach cannot be carried out at arbitrarily high T_E . The longer T_E , the greater the signal attenuation due to transverse relaxation, which ultimately changes the compartmental weighting of the frequency distribution. In our simulations, we found T_E up to 80 ms could estimate the mean magnetic field at 7T reasonably, by sampling the SE signal after T_E at times ΔT_E up to 20 ms. The maximum timings used in both MGE and ASE signals depends ultimately on the variance in the frequency shifts across the different axons. This is why SHAM-49-ipsi produced the best estimates, as here only cingulum was included. We therefore propose that susceptibility estimation may benefit from using the signal phase of an asymmetric spin echo to avoid contributions from myelin water. In addition, a dMRI dataset with high b-values (around $b = 5 \text{ ms}/\mu\text{m}^2$ or higher in-vivo) and multiple gradient directions (around 60 directions) should be acquired with a diffusion time Δ around 40 ms, which can be achieved in around 10-20 minutes on a 3T clinical scanner.

6| Conclusion

We performed Monte-Carlo simulations in mesoscopically sized samples of white matter axons to test if structural information obtained with diffusion MRI can be used to account for the effect of microstructure probed with the susceptibility-induced Larmor frequency shift of the gradient echo signal. We found that by fitting the Standard Model of diffusion in white matter to the simulated pulsed gradient spin-echo signal, the estimated fiber orientation distribution function could successfully be used to account for the orientation dependence of the Larmor frequency shift with respect to the B_0 field. Our simulations also showed that intra-axonal axial kurtosis affects the diffusion-weighted MRI signal and should not be neglected.

Our work is an important step towards validating the use of dMRI information to account for sub-voxel frequency shift caused by structural anisotropy of WM, which is crucial for robust

susceptibility estimation – with the end goal of developing a unified model of both susceptibility and diffusion effects in MRI.

7| Acknowledgements

This study is funded by the Independent Research Fund (10.46540/3103-00144B). Codes are available upon reasonable request to the corresponding author.

8| Supporting Material

Validation of Monte-Carlo simulation

Here we present a set of Monte-Carlo (MC) simulations to ensure that the MC simulations in the main manuscript are trustworthy.

A) Single cylinder

We considered the time dependent axial and radial diffusivity $D_{\parallel}(t), D_{\perp}(t)$ and kurtosis $K_{\parallel}(t), K_{\perp}(t)$

$$D(\hat{\mathbf{n}}; t) = \frac{\langle (\mathbf{r} \cdot \hat{\mathbf{n}})^2 \rangle}{2t} \quad (20)$$

$$K(\hat{\mathbf{n}}; t) = \frac{\langle (\mathbf{r} \cdot \hat{\mathbf{n}})^4 \rangle}{\langle (\mathbf{r} \cdot \hat{\mathbf{n}})^2 \rangle^2} - 3 \quad (21)$$

at diffusion time t of a perfect cylinder and compared it with known analytical solutions. The subscripts \parallel, \perp correspond to using $\hat{\mathbf{n}}$ parallel or perpendicular to the cylinder axis, respectively. The purpose of the simulation is also to check that the axial diffusivity D_{\parallel} is biased from using rejection sampling, i.e., if rejecting the step when a particle collides with the cylinder boundary reduces the diffusivity depending on the surface-to-volume ratio S/V and diffusion step length δl . We discretized a single cylinder with a radius of $1 \mu\text{m}$ and length $68 \mu\text{m}$ (comparable S/V to the real axons) inside a 3D grid with a resolution of $0.1 \mu\text{m}^3$ – similar to the large-scale simulations. Around $5 \cdot 10^3$ particles inside the cylinder was used to have the same density of particles as in the axons. Figure 11 shows the axial and radial diffusivities $D_{\parallel}(t), D_{\perp}(t)$ and kurtoses $K_{\parallel}(t), K_{\perp}(t)$ from both MC and analytical solutions. We also plotted the analytical solutions for $D_{\perp}(t)$ and $K_{\perp}(t)$ for comparison with MC, while for $D_{\parallel}(t)$, we also plot the time-averaged axial diffusivity $\langle D_{\parallel} \rangle_t$ and the axial diffusivity, expected to be biased according to

$$D'_0 \approx D_0 \left(1 - \frac{3}{16} \frac{S}{V} \delta l \right) \quad (22)$$

due to using rejection sampling, where $\delta l S/V = 0.94$. We see in Figure 11 that $\langle D_{\parallel} \rangle_t \approx 0.94 D_0 \approx D'_0$ was biased at around 6% in agreement with the expectation. The axial kurtosis quickly converged to zero as expected, while the radial diffusivity and kurtosis followed the analytical solution. The axial variance is around 2%, which is indicative of the low number of particles inside the cylinder. However, increasing the number of axons lowers the variance. Hence, if a single axon was to be considered, the number of particles should be increased, but pooling the results over many, we found this particle density to be sufficient, as will be evident in the next section.

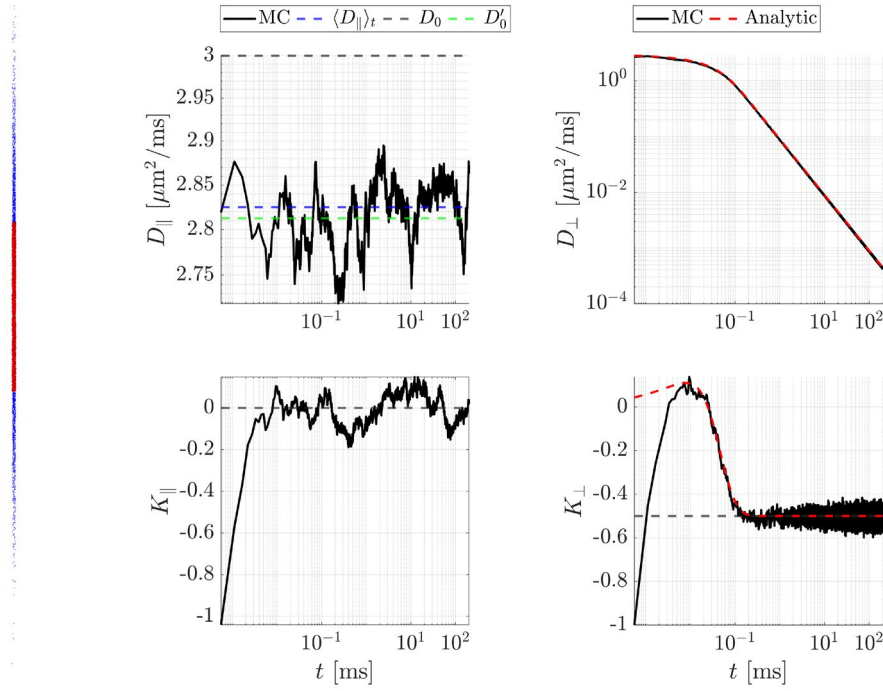


Figure 11 – Monte-Carlo simulation of intra-cylindrical diffusion: To the left, red dots indicate particles positions inside the cylinder; where a particle passing through one end comes out the other end. Blue dots represent the actual displacement at $t = 200$ ms. First column shows the axial diffusivity $D_{\parallel}(t)$ and kurtosis $K_{\parallel}(t)$, while the second column shows the radial diffusivity and kurtosis $D_{\perp}(t), K_{\perp}(t)$, respectively, including analytical solutions in red.

b) Realistic axons

Here we simulated $D_{\parallel}(t), D_{\perp}(t), K_{\parallel}(t), K_{\perp}(t)$ in realistic axons to investigate their asymptotic behaviors for $t \rightarrow \infty$. In particular, the power law scaling should be $D_{\parallel}(t), K_{\parallel}(t) \sim 1/\sqrt{t}$ while $D_{\perp}(t), K_{\perp}(t) \sim 1/t$ for $t \rightarrow \infty$.^{84–86} We compute the time dependence for the diffusion and kurtosis parameters for 945 different axons from the cingulum bundle in their own frame of reference $\hat{\mathbf{n}}_i$ for the i 'th axon. The axial direction $\hat{\mathbf{n}}_i$ was chosen by averaging the tangent directions of the center-of-mass line of an axon, coarse-grained by a Gaussian filter corresponding to a diffusion length of $25 \mu\text{m}$. We computed the total diffusivity and kurtosis $D(t), K(t)$ in the common frame of reference defined as $\hat{\mathbf{n}} = \sum_i f_i \hat{\mathbf{n}}_i$ to include the natural orientation dispersion

$$D(t) = \sum_i f_i D_i(\hat{\mathbf{n}}_i; t) \quad (23)$$

$$K(t) = \frac{1}{D(t)^2} \sum_i f_i (D_i(\hat{\mathbf{n}}_i; t) - D(t))^2 + f_i D_i(\hat{\mathbf{n}}_i; t)^2 K_i(\hat{\mathbf{n}}_i; t) \quad (24)$$

We considered here diffusion times up to $t = 400$ ms. We also calculated with a density of particles of either 72 particles/ μm^3 or 572 particles/ μm^3 , where the first corresponds to the density used in the main simulations. This is to demonstrate that we do not need a lot of particles inside every axon to produce robust results. This is because we are not interested in the diffusivity of individual axons but rather the behavior over the entire population. Figure 12 shows the decay of $D_{\parallel}(t), D_{\perp}(t)$ and kurtoses $K_{\parallel}(t), K_{\perp}(t)$ for long diffusion times for individual axons and all of them. Figure 12A is for axons in their own reference frame, while Figure 12B is in their common reference frame. Our results agree with previous studies^{84–86} when every axon is considered in their own reference frame. Surprisingly, when we compute $K_{\perp}(t)$ in the common frame of reference, it diverges even though $K_i(\hat{\mathbf{n}}_i; t)$ does not. Hence the divergence comes from the diffusion variance from certain axons $D_i(\hat{\mathbf{n}}_i; t) - D(t)$ converge to 0 at a slower rate as $D(t)$. Figure 13 shows the contribution to $K_{\perp}(t)$ from $D_i(\hat{\mathbf{n}}_i; t)$ when calculated in the common reference frame, and in the individual. Axons that deviate from the main orientation can clearly contribute to the diffusion variance such that $K_{\perp}(t)$ appears to diverge within the considered time scale. Looking at the total parallel kurtosis $K_{\parallel}(t)$ in the individual axon reference frame, we observed that it remains non-zero even for very high diffusion times. For that reason, we also considered including W_{\parallel} when fitting the Standard Model of diffusion to the MC simulated PGSE signal.

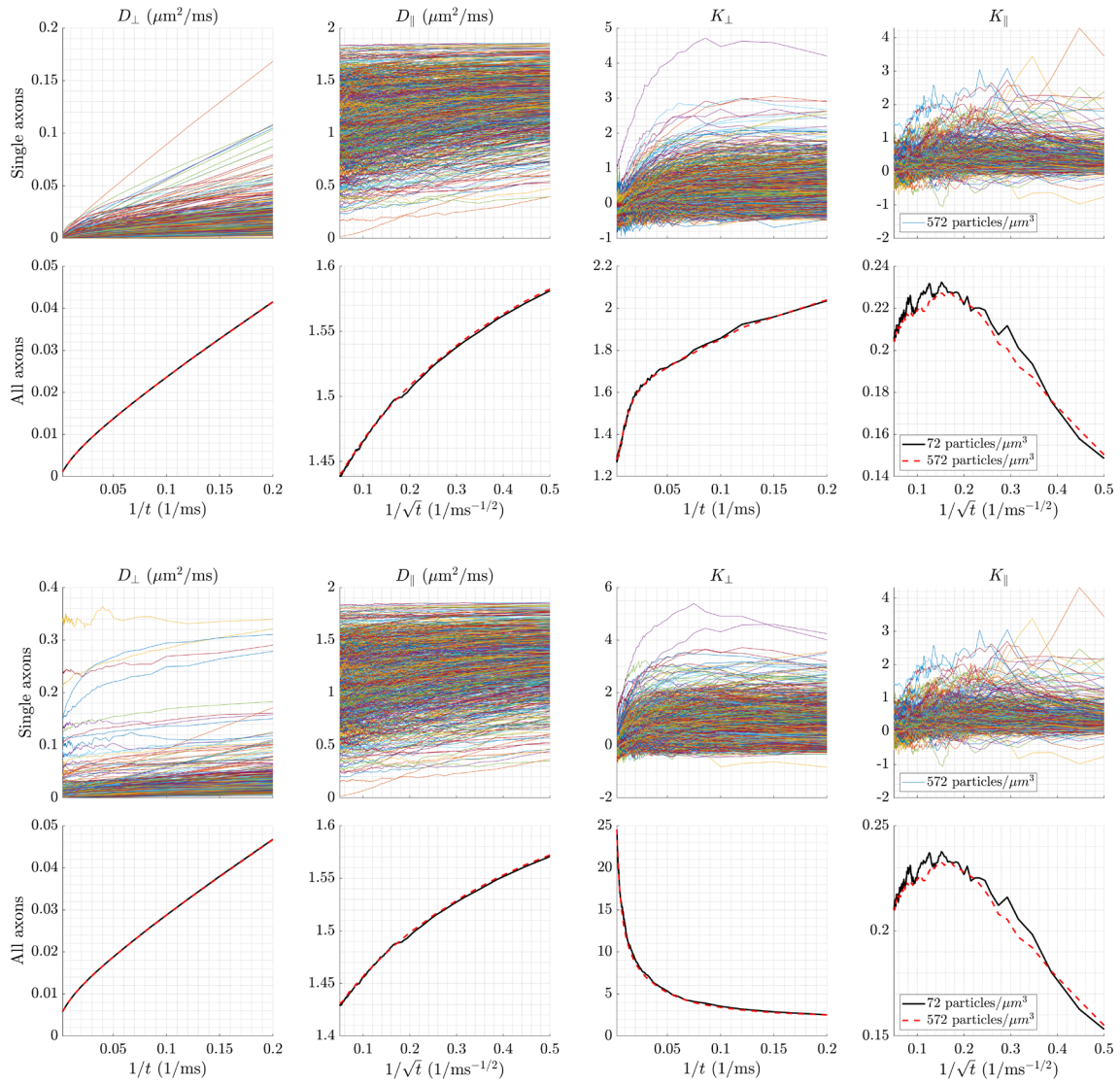


Figure 12 – Monte-Carlo simulation of intra-axonal diffusion and kurtosis: The axial diffusivity $D_{\parallel}(t)$ and kurtosis $K_{\parallel}(t)$ are plotted as a function of $1/t$ while $D_{\perp}(t), K_{\perp}(t)$ are plotted as a function of $1/\sqrt{t}$. The first and third row show single axons, while the second and fourth row show all. The two first rows show when the diffusivity and kurtosis are calculated with axons in their own reference frames, while the third and fourth row show for axons calculated in their common reference frame.

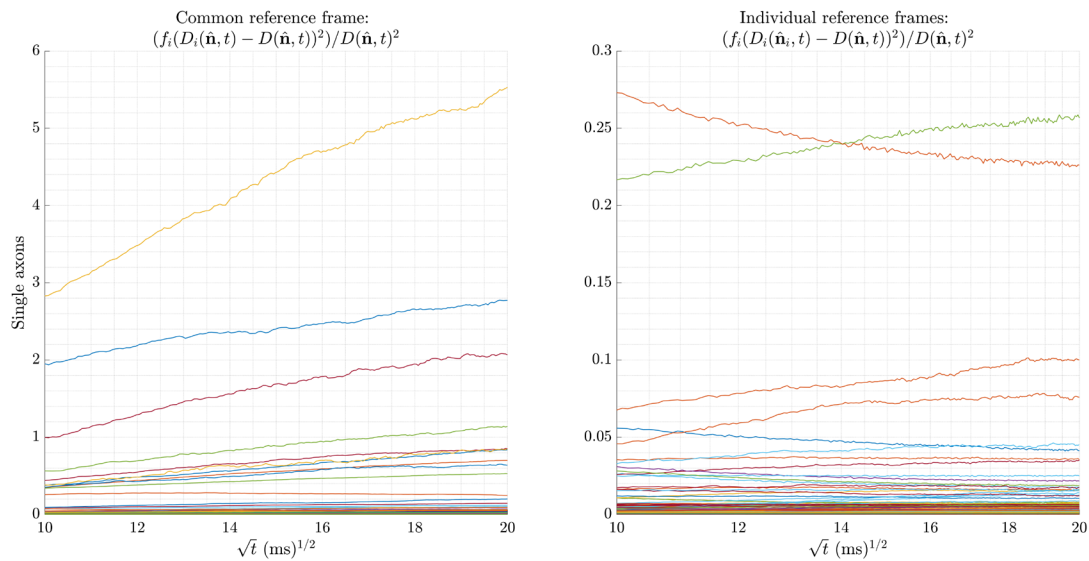


Figure 13 – Contribution to intra-axonal diffusion variance from each axon: The first plot shows the individual contributions to the diffusion variance contribution to the kurtosis from all 945 axons calculated in their common reference frame. Axons deviating from the common reference frame decays slower than the total mean diffusivity $D(\hat{\mathbf{n}}, t)$, which leads to a diverging kurtosis contribution. The second plot shows each contribution to the diffusion variance in each axon's own reference frame. Here, most axon tend towards zero.

9| References

1. Duyn J. MR susceptibility imaging. *J Magn Reson.* 2013;229:198-207. doi:10.1016/j.jmr.2012.11.013
2. Novikov DS, Fieremans E, Jespersen SN, Kiselev VG. Quantifying brain microstructure with diffusion MRI: Theory and parameter estimation. *NMR Biomed.* 2019;32(4):e3998. doi:10.1002/NBM.3998
3. Liao Y, Coelho S, Chen J, et al. Mapping tissue microstructure of brain white matter in vivo in health and disease using diffusion MRI. *Imaging Neurosci.* 2024;2:1-17. doi:10.1162/IMAG_A_00102/119636/MAPPING-TISSUE-MICROSTRUCTURE-OF-BRAIN-WHITE
4. Jelescu IO, Zurek M, Winters K V., et al. In vivo quantification of demyelination and recovery using compartment-specific diffusion MRI metrics validated by electron microscopy. *Neuroimage.* 2016;132:104-114. doi:10.1016/J.NEUROIMAGE.2016.02.004
5. Jelescu IO, Veraart J, Adisetiyo V, Milla SS, Novikov DS, Fieremans E. One diffusion acquisition and different white matter models: How does microstructure change in human early development based on WMTI and NODDI? *Neuroimage.* 2015;107:242-256. doi:10.1016/J.NEUROIMAGE.2014.12.009
6. Benitez A, Fieremans E, Jensen JH, et al. White matter tract integrity metrics reflect the vulnerability of late-myelinating tracts in Alzheimer's disease. *NeuroImage Clin.* 2014;4:64-71. doi:10.1016/J.NICL.2013.11.001
7. Novikov SH, Ferris JA, Helpert DS, et al. Novel White Matter Tract Integrity Metrics Sensitive to Alzheimer Disease Progression. *Am J Neuroradiol.* 2013;34(11):2105-2112. doi:10.3174/AJNR.A3553

8. Yablonskiy DA, Haacke EM. Theory of NMR signal behavior in magnetically inhomogeneous tissues: The static dephasing regime. *Magn Reson Med.* 1994;32(6):749-763. doi:10.1002/mrm.1910320610
9. Yablonskiy DA, Sukstanskii AL. Generalized Lorentzian Tensor Approach (GLTA) as a biophysical background for quantitative susceptibility mapping. *Magn Reson Med.* 2015;73(2):757-764. doi:10.1002/mrm.25538
10. He X, Yablonskiy DA. Biophysical mechanisms of phase contrast in gradient echo MRI. *Proc Natl Acad Sci U S A.* 2009;106(32):13558-13563. doi:10.1073/pnas.0904899106
11. Ruh A, Scherer H, Kiselev VG. The Larmor frequency shift in magnetically heterogeneous media depends on their mesoscopic structure. *Magn Reson Med.* 2018;79(2):1101-1110. doi:10.1002/mrm.26753
12. Kiselev VG. Larmor frequency in heterogeneous media. *J Magn Reson.* 2019;299:168-175. doi:10.1016/j.jmr.2018.12.008
13. Sandgaard AD, Kiselev VG, Henriques RN, Shemesh N, Jespersen SN. Incorporating the effect of white matter microstructure in the estimation of magnetic susceptibility in ex vivo mouse brain. *Magn Reson Med.* Published online September 29, 2023. doi:10.1002/MRM.29867
14. Sandgaard AD, Shemesh N, Kiselev VG, Jespersen SN. Larmor frequency shift from magnetized cylinders with arbitrary orientation distribution. *NMR Biomed.* 2023;36(3):e4859. doi:10.1002/nbm.4859
15. Chen J, Gong NJ, Chaim KT, Otaduy MCG, Liu C. Decompose quantitative susceptibility mapping (QSM) to sub-voxel diamagnetic and paramagnetic components based on gradient-echo MRI data. *Neuroimage.* 2021;242:118477. doi:10.1016/J.NEUROIMAGE.2021.118477
16. Feng R, Cao S, Zhuang J, et al. An improved asymmetric susceptibility tensor imaging model with frequency offset correction. *Magn Reson Med.* Published online October 27, 2022. doi:10.1002/MRM.29494
17. Gkotsoulias DG, Müller R, Jäger C, et al. High Angular Resolution Susceptibility Imaging and Estimation of Fiber Orientation Distribution Functions in Primate Brain. *Neuroimage.* 2023;276:120202. doi:10.1016/J.NEUROIMAGE.2023.120202
18. Li W, Wu B, Avram A V., Liu C. Magnetic susceptibility anisotropy of human brain in vivo and its molecular underpinnings. *Neuroimage.* 2012;59(3):2088-2097. doi:10.1016/J.NEUROIMAGE.2011.10.038
19. Liu C. Susceptibility tensor imaging. *Magn Reson Med.* 2010;63(6):1471-1477. doi:10.1002/mrm.22482
20. Liu C, Li W, Johnson GA, Wu B. High-field (9.4 T) MRI of brain dysmyelination by quantitative mapping of magnetic susceptibility. *Neuroimage.* 2011;56(3):930-938. doi:10.1016/J.NEUROIMAGE.2011.02.024
21. Lee J, Shmueli K, Kang BT, et al. The contribution of myelin to magnetic susceptibility-weighted contrasts in high-field MRI of the brain. *Neuroimage.* 2012;59(4):3967-3975. doi:10.1016/J.NEUROIMAGE.2011.10.076
22. Shin HG, Lee J, Yun YH, et al. χ -separation: Magnetic susceptibility source separation toward iron and myelin mapping in the brain. *Neuroimage.* 2021;240:118371. doi:10.1016/J.NEUROIMAGE.2021.118371
23. Duyn JH, Van Gelderen P, Li TQ, De Zwart JA, Koretsky AP, Fukunaga M. High-field MRI of brain cortical substructure based on signal phase. *Proc Natl Acad Sci U S A.*

- 2007;104(28):11796-11801. doi:10.1073/PNAS.0610821104/ASSET/98E47EFB-3057-4B46-9370-42FDD1888E60/ASSETS/GRAPHIC/ZPQ02807-6637-M08.JPEG
24. Mitra PP, Sen PN, Schwartz LM, Le Doussal P. Diffusion propagator as a probe of the structure of porous media. *Phys Rev Lett*. 1992;68(24):3555. doi:10.1103/PhysRevLett.68.3555
 25. Reichenbach JR, Schweser F, Serres B, Deistung A. Quantitative Susceptibility Mapping: Concepts and Applications. *Clin Neuroradiol*. 2015;25(2):225-230. doi:10.1007/S00062-015-0432-9/FIGURES/3
 26. Deistung A, Schweser F, Reichenbach JR. Overview of quantitative susceptibility mapping. *NMR Biomed*. 2017;30(4):e3569. doi:10.1002/nbm.3569
 27. Sandgaard AD, Shemesh N, Østergaard L, Kiselev VG, Jespersen SN. The Larmor frequency shift of a white matter magnetic microstructure model with multiple sources. *NMR Biomed*. Published online 2024:e5150. doi:10.1002/NBM.5150
 28. Andersson M, Kjer HM, Rafael-Patino J, et al. Axon morphology is modulated by the local environment and impacts the noninvasive investigation of its structure–function relationship. *Proc Natl Acad Sci U S A*. 2021;117(52):33649-33659. doi:10.1073/PNAS.2012533117
 29. Weisskoff R, Zuo CS, Boxerman JL, Rosen BR. Microscopic susceptibility variation and transverse relaxation: Theory and experiment. *Magn Reson Med*. 1994;31(6):601-610. doi:10.1002/MRM.1910310605
 30. Lipinski HG. Monte Carlo simulation of extracellular diffusion in brain tissues. *Phys Med Biol*. 1990;35(3):441. doi:10.1088/0031-9155/35/3/012
 31. Balinov B, Jönsson B, Linse P, Söderman O. The NMR Self-Diffusion Method Applied to Restricted Diffusion. Simulation of Echo Attenuation from Molecules in Spheres and between Planes. *J Magn Reson Ser A*. 1993;104(1):17-25. doi:10.1006/JMRA.1993.1184
 32. Ginsburger K, Matuschke F, Poupon F, Mangin JF, Axer M, Poupon C. MEDUSA: A GPU-based tool to create realistic phantoms of the brain microstructure using tiny spheres. *Neuroimage*. 2019;193:10-24. doi:10.1016/J.NEUROIMAGE.2019.02.055
 33. Ginsburger K, Poupon F, Beaujoin J, et al. Improving the realism of white matter numerical phantoms: A step toward a better understanding of the influence of structural disorders in diffusion MRI. *Front Phys*. 2018;5(FEB):334547. doi:10.3389/FPHY.2018.00012/BIBTEX
 34. Rafael-Patino J, Girard G, Truffet R, Pizzolato M, Thiran JP, Caruyer E. The Microstructural Features of the Diffusion-Simulated Connectivity (DiSCo) Dataset. *Lect Notes Comput Sci (including Subser Lect Notes Artif Intell Lect Notes Bioinformatics)*. 2021;13006 LNCS:159-170. doi:10.1007/978-3-030-87615-9_14/FIGURES/6
 35. Novikov DS, Fieremans E, Jensen JH, Helpert JA. Random walk with barriers: Diffusion restricted by permeable membranes. Published online April 15, 2010. doi:10.1038/nphys1936
 36. Lin M, He H, Schifitto G, Zhong J. Simulation of changes in diffusion related to different pathologies at cellular level after traumatic brain injury. *Magn Reson Med*. 2016;76(1):290-300. doi:10.1002/MRM.25816
 37. Villarreal-Haro JL, Gardier R, Canales-Rodríguez EJ, et al. CACTUS: a computational framework for generating realistic white matter microstructure substrates. *Front Neuroinform*. 2023;17:1208073. doi:10.3389/FNINF.2023.1208073/BIBTEX
 38. Harkins KD, Does MD. Simulations on the influence of myelin water in diffusion-weighted imaging. *Phys Med Biol*. 2016;61(13):4729-4745. doi:10.1088/0031-9155/61/13/4729
 39. Gudbjartsson H, Patz S. NMR Diffusion Simulation Based on Conditional Random Walk.

- IEEE Trans Med Imaging*. 1995;14(4):636-642. doi:10.1109/42.476105
40. Rafael-Patino J, Romascano D, Ramirez-Manzanares A, Canales-Rodríguez EJ, Girard G, Thiran JP. Robust Monte-Carlo Simulations in Diffusion-MRI: Effect of the Substrate Complexity and Parameter Choice on the Reproducibility of Results. *Front Neuroinform*. 2020;14:457195. doi:10.3389/FNINF.2020.00008/BIBTEX
 41. Ruh A, Kiselev VG. Larmor frequency dependence on structural anisotropy of magnetically heterogeneous media. *J Magn Reson*. 2019;307:106584. doi:10.1016/j.jmr.2019.106584
 42. Chen WC, Foxley S, Miller KL. Detecting microstructural properties of white matter based on compartmentalization of magnetic susceptibility. *Neuroimage*. 2013;70:1-9. doi:10.1016/j.neuroimage.2012.12.032
 43. Xu T, Foxley S, Kleinnijenhuis M, Chen WC, Miller KL. The effect of realistic geometries on the susceptibility-weighted MR signal in white matter. *Magn Reson Med*. 2018;79(1):489-500. doi:10.1002/mrm.26689
 44. Palombo M, Ligneul C, Hernandez-Garzon E, Valette J. Can we detect the effect of spines and leaflets on the diffusion of brain intracellular metabolites? *Neuroimage*. 2018;182:283-293. doi:10.1016/J.NEUROIMAGE.2017.05.003
 45. Balls GT, Frank LR. A simulation environment for diffusion weighted MR experiments in complex media. *Magn Reson Med*. 2009;62(3):771-778. doi:10.1002/MRM.22033
 46. Frank LR, Balls G, Rapp JL. Simulation of the MRI measurement of diffusion in realistic neural tissue models. In: *Annual International Conference of the IEEE Engineering in Medicine and Biology - Proceedings*. ; 2006:2243-2244. doi:10.1109/IEMBS.2006.259547
 47. Nilsson M, Lätt J, Ståhlberg F, van Westen D, Hagglätt H. The importance of axonal undulation in diffusion MR measurements: a Monte Carlo simulation study. *NMR Biomed*. 2012;25(5):795-805. doi:10.1002/NBM.1795
 48. Callaghan R, Alexander DC, Palombo M, Zhang H. ConFiG: Contextual Fibre Growth to generate realistic axonal packing for diffusion MRI simulation. *Neuroimage*. 2020;220:117107. doi:10.1016/J.NEUROIMAGE.2020.117107
 49. Li JR, Nguyen HT, Van Nguyen D, Haddar H, Coatléven J, Le Bihan D. Numerical study of a macroscopic finite pulse model of the diffusion MRI signal. *J Magn Reson*. 2014;248:54-65. doi:10.1016/J.JMR.2014.09.004
 50. Ruiz Barlett V, Hoyuelos M, Martín HO. Monte Carlo simulation with fixed steplength for diffusion processes in nonhomogeneous media. *J Comput Phys*. 2013;239:51-56. doi:10.1016/J.JCP.2012.12.029
 51. Nguyen D Van, Li JR, Grebenkov D, Le Bihan D. A finite elements method to solve the Bloch–Torrey equation applied to diffusion magnetic resonance imaging. *J Comput Phys*. 2014;263:283-302. doi:10.1016/J.JCP.2014.01.009
 52. Ruh A, Emerich P, Scherer H, Novikov DS, Kiselev VG. Observation of magnetic structural universality using transverse NMR relaxation. Published online October 11, 2018. doi:10.48550/arxiv.1810.04847
 53. Winther S, Lundell H, Rafael-Patiño J, Andersson M, Thiran JP, Dyrby TB. Susceptibility-induced internal gradients reveal axon morphology and cause anisotropic effects in the dMRI signal. *bioRxiv*. Published online May 2, 2023:2023.05.01.538981. doi:10.1101/2023.05.01.538981
 54. Novikov DS, Kiselev VG. Transverse NMR relaxation in magnetically heterogeneous media. *J Magn Reson*. 2008;195(1):33-39. doi:10.1016/j.jmr.2008.08.005

55. Novikov DS, Reisert M, Kiselev VG. Effects of mesoscopic susceptibility and transverse relaxation on diffusion NMR. *J Magn Reson.* 2018;293:134-144. doi:10.1016/J.JMR.2018.06.007
56. Abdollahzadeh A, Belevich I, Jokitalo E, Sierra A, Tohka J. DeepACSON automated segmentation of white matter in 3D electron microscopy. *Commun Biol* 2021 41. 2021;4(1):1-14. doi:10.1038/s42003-021-01699-w
57. Abdollahzadeh A, Belevich I, Jokitalo E, Tohka J, Sierra A. Automated 3D Axonal Morphometry of White Matter. *Sci Reports* 2019 91. 2019;9(1):1-16. doi:10.1038/s41598-019-42648-2
58. Stejskal EO, Tanner JE. Spin Diffusion Measurements: Spin Echoes in the Presence of a Time Dependent Field Gradient. *Cit J Chem Phys.* 1965;42:288. doi:10.1063/1.1695690
59. Lee HHH, Yaros K, Veraart J, et al. Along-axon diameter variation and axonal orientation dispersion revealed with 3D electron microscopy: implications for quantifying brain white matter microstructure with histology and diffusion MRI. *Brain Struct Funct.* 2019;224(4):1469-1488. doi:10.1007/s00429-019-01844-6
60. Lee HH, Fieremans E, Novikov DS. Realistic Microstructure Simulator (RMS): Monte Carlo simulations of diffusion in three-dimensional cell segmentations of microscopy images. *J Neurosci Methods.* 2021;350:109018. doi:10.1016/J.JNEUMETH.2020.109018
61. Luo J, He X, Yablonskiy DA. Magnetic susceptibility induced white matter MR signal frequency shifts—experimental comparison between Lorentzian sphere and generalized Lorentzian approaches. *Magn Reson Med.* 2014;71(3):1251-1263. doi:10.1002/MRM.24762
62. Wharton S, Bowtell R. Effects of white matter microstructure on phase and susceptibility maps. *Magn Reson Med.* 2015;73(3):1258-1269. doi:10.1002/mrm.25189
63. Jones DK, Horsfield MA, Simmons A. Optimal strategies for measuring diffusion in anisotropic systems by magnetic resonance imaging. *Magn Reson Med.* 1999;42(3):515-525. doi:10.1002/(SICI)1522-2594(199909)42:3<515::AID-MRM14>3.0.CO;2-Q
64. Olesen JL, Østergaard L, Shemesh N, Jespersen SN. Beyond the diffusion standard model in fixed rat spinal cord with combined linear and planar encoding. *Neuroimage.* 2021;231:117849. doi:10.1016/J.NEUROIMAGE.2021.117849
65. Schwarz G. Estimating the Dimension of a Model. <https://doi.org/10.1214/aos/1176344136>. 1978;6(2):461-464. doi:10.1214/AOS/1176344136
66. Kass RE, Raftery AE. Bayes factors. *J Am Stat Assoc.* 1995;90(430):773-795. doi:10.1080/01621459.1995.10476572
67. Fisher NI, Lewis T, Embleton BJJ. *Statistical Analysis of Spherical Data.* Cambridge University Press; 1987. doi:10.1017/CBO9780511623059
68. Lee HH, Papaioannou A, Kim SL, Novikov DS, Fieremans E. A time-dependent diffusion MRI signature of axon caliber variations and beading. *Commun Biol* 2020 31. 2020;3(1):1-13. doi:10.1038/s42003-020-1050-x
69. Möller HE, Bossoni L, Connor JR, et al. Iron, Myelin, and the Brain: Neuroimaging Meets Neurobiology. *Trends Neurosci.* 2019;42(6):384-401. doi:10.1016/J.TINS.2019.03.009
70. Anders Dyhr S, Jespersen SN. Towards a Standard Model of Diffusion in White Matter with Phase and Relaxation – A Monte-Carlo Study. In: *Proceedings of the Annual Meeting of the ISMRM Online Conference.* ; 2024:#0589. <https://submissions.mirasmart.com/ISMRM2024/Itinerary/ConferenceMatrixEventDetail.aspx?ses=PP-32>

71. Shapson-Coe A, Januszewski M, Berger DR, et al. A connectomic study of a petascale fragment of human cerebral cortex. *bioRxiv*. Published online November 25, 2021:2021.05.29.446289. doi:10.1101/2021.05.29.446289
72. Westin CF, Knutsson H, Pasternak O, et al. Q-space trajectory imaging for multidimensional diffusion MRI of the human brain. *Neuroimage*. 2016;135:345-362. doi:10.1016/J.NEUROIMAGE.2016.02.039
73. Sandgaard AD, Kiselev VG, Shemesh N, Jespersen SN. Incorporating susceptibility effects into the standard model of diffusion in white matter. In: *Proceedings of the International Society of Magnetic Resonance in Medicine*. ISMRM; 2023:#0975. <https://www.ismrm.org/23/program-files/PP-11.htm>
74. Sati P, van Gelderen P, Silva AC, et al. Micro-compartment specific T2* relaxation in the brain. *Neuroimage*. 2013;77:268-278. doi:10.1016/J.NEUROIMAGE.2013.03.005
75. Van Gelderen P, De Zwart JA, Lee J, Sati P, Reich DS, Duyn JH. Nonexponential T2* decay in white matter. *Magn Reson Med*. 2012;67(1):110-117. doi:10.1002/mrm.22990
76. Nam Y, Lee J, Hwang D, Kim DH. Improved estimation of myelin water fraction using complex model fitting. *Neuroimage*. 2015;116:214-221. doi:10.1016/J.NEUROIMAGE.2015.03.081
77. Lee J, Hyun JW, Lee J, et al. So You Want to Image Myelin Using MRI: An Overview and Practical Guide for Myelin Water Imaging. *J Magn Reson Imaging*. 2021;53(2):360-373. doi:10.1002/JMRI.27059
78. Duyn JH. Frequency shifts in the myelin water compartment. *Magn Reson Med*. 2014;71(6):1953-1955. doi:10.1002/mrm.24983